2. GLOBAL CLIMATE—K. M. Willett, L. V. Alexander, and P. W. Thorne, Eds.

a. Summary—L. V. Alexander

In 2009, a transition from La Niña to El Niño dominated anomalies in many climate variables from the surface to the lower stratosphere. Averaged over the year, there was large-scale surface and tropospheric warmth and stratospheric coolness, except in the Arctic where positive annual anomalies were dominated by the largest stratospheric warming in January in the 50-year record (Plate 2.1). The ENSO transition, which occurred during the boreal summer, contributed to 2009 being ranked in the top 10 warmest years globally, about 0.1°C warmer than 2008. Global average surface temperatures during the last three decades have been progressively warmer than all earlier decades, making 2000-09 (the 2000s) the warmest decade in the instrumental record. The 2000s were also the warmest decade on record in the lower troposphere, being about 0.6°C warmer than the 1960s and 0.2°C warmer than the 1990s. The decadal warming has been particularly apparent in the mid- and high-latitude regions of the Northern Hemisphere. This chapter also includes a sidebar on the veracity of and supporting evidence for the surface temperature records following much recent discussion in the popular media. Globally averaged surface temperature anomalies are shown to be robust given the close agreement between independently-derived datasets and strong corroborative evidence across a wide range of other climate variables.

Cloud and moisture increased in the tropical Pacific although there was no distinctive ENSO signature in annual surface pressure, owing to the cancelling effect of the shift from La Niña to El Niño. Preliminary data indicate a high probability that 2009 will be the 19th consecutive year that glaciers have lost mass. Precipitation anomalies were variable but most marked was a drying over the tropical Atlantic coincident with the position of ITCZ. Greenhouse gas concentrations continued to rise in 2009, with CO_2 increasing at a rate above the 1978 to 2008 average. Ozone-depleting gas concentrations continued to decline although some halogens such as hydrochlorofluorocarbons are increasing globally. Total-column ozone concentrations are still well below pre-1980 levels but have seen a recent reduction in the rate of decline, while upper stratospheric ozone has shown continued signs of ongoing slow recovery in 2009.

This year's global chapter incorporates additional climate variables over previous years. There is not a section on land cover because there are limited annual updates to this variable. Land cover will be included in future summaries as updates become available. Advances and improvements in technology have enhanced our ability to monitor the Earth's climate using methods such as Global Positioning System Radio Occultation (see sidebar), which can be used to measure multiple meteorological parameters. Also included this year are lake levels (a proxy for precipitation changes over a catchment basin) and biomass burning (a proxy for land cover change and fire disturbance). In addition, for the first time, data from a reanalysis product have been included. This was possible through substantial recent improvements in reanalysis products. There is exciting potential to use analyses from these observing systems and combined products to enhance future global summaries.

Publicly available datasets used in this chapter are included in Table 2.1

b. Temperatures

1) Introduction of reanalysis data—P. W. Thorne

This year for the first time there are fields from a reanalysis product within the global chapter. Reanalyses consist of modern day data assimilation schemes fed with all available historical observations. They produce spatially complete fields of a whole suite of meteorological parameters—both measured parameters and derived parameters such as potential vorticity. Papers documenting reanalyses are some of the most highly cited (e.g., Kalnay et al. 1996; Uppala et al. 2005), attesting to the high utility of reanalyses for a myriad of applications. They have not been included in the global chapter of *State of the Climate* to date because of well documented concerns about the ability of early reanalysis products to characterize long-term trends. The third generation of reanalysis products include substantial improvements as each successive effort has learned from previous efforts and taken advantage of developments in the sphere of weather forecasting. The ability of these much newer reanalysis products to characterize long-term changes in at least a subset of meteorological parameters has now been documented (e.g., Simmons et al. 2010). As a first step towards their more comprehensive inclusion in future *State of the Climate* reports this year there are results from the European Centre for Medium Range Forecasts (ECMWF) ERA-40 and ERA-interim reanalyses (Simmons et al. 2010) incorporated into the three temperature sections. It is hoped that in future years these can be augmented by other third generation reanalysis products from NASA (MERRA, Bosilovich 2008), JRA-55 from the Japan Meteorologi-

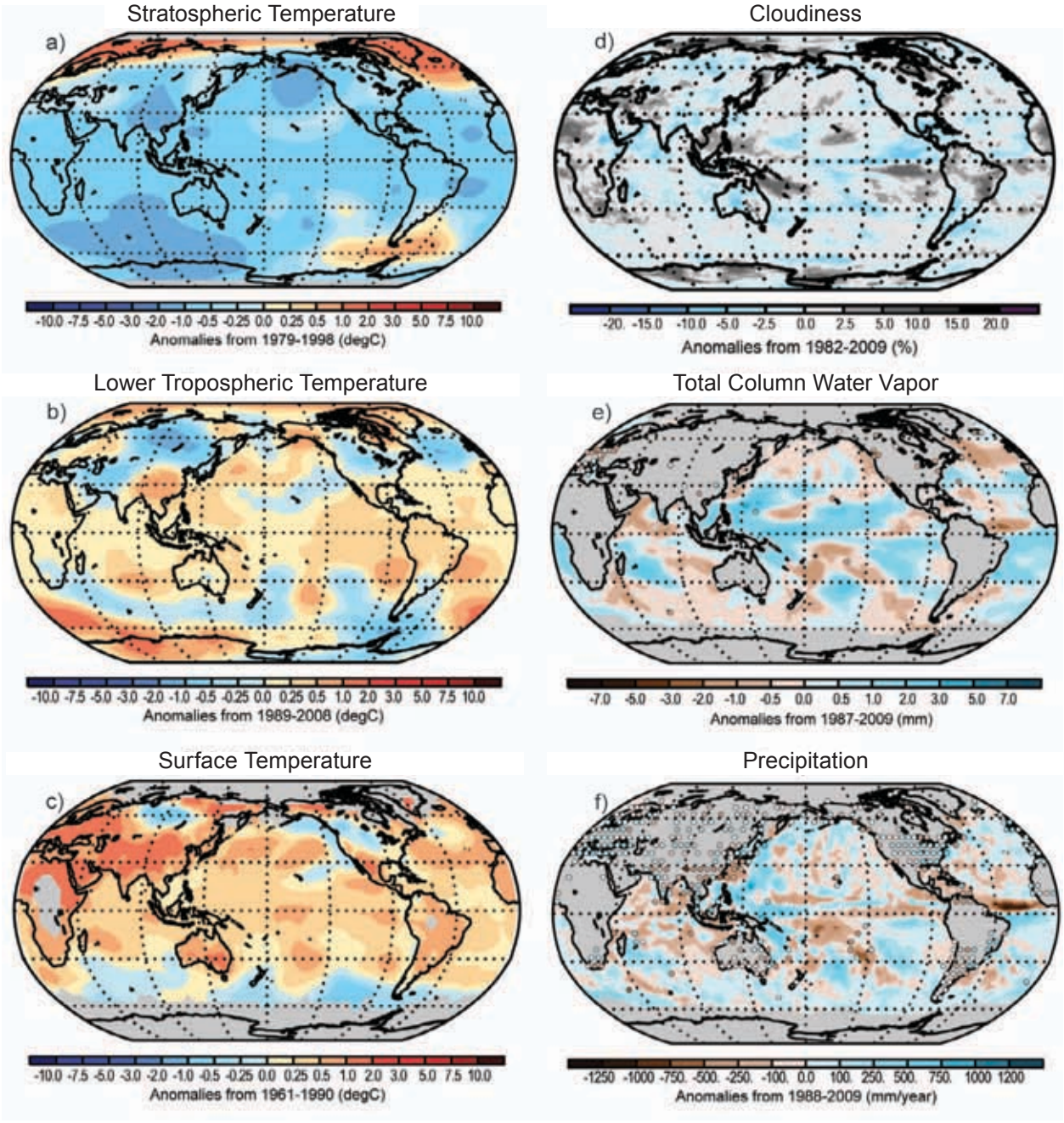

Plate 2.1. Global annual anomaly maps for those variables for which it is possible to create a meaningful 2009 anomaly estimate. Climatologies differ among variables, but spatial patterns should largely dominate over choices of climatology period. Dataset sources/names are as follows: lower stratospheric temperature (RSS MSU); lower tropospheric temperature (ERA-interim); surface temperature (NOAA/NCDC); cloudiness (PATMOS-x); total column water vapor (SSM/I over ocean, ground based GPS over land); precipitation [RSS over ocean, GHCN (gridded) over land]; river discharge (authors); mean sea level pressure (HadSLP2r); wind speed (AMSR-E); ozone (GOME2); FAPAR (SeaWIFS); biomass burning (GEMS/MACC). See relevant section text and figures for more details.

River Discharge Continent Runoff

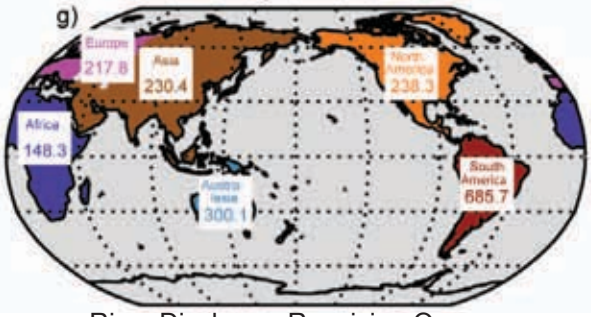

River Discharge Receiving Oceans

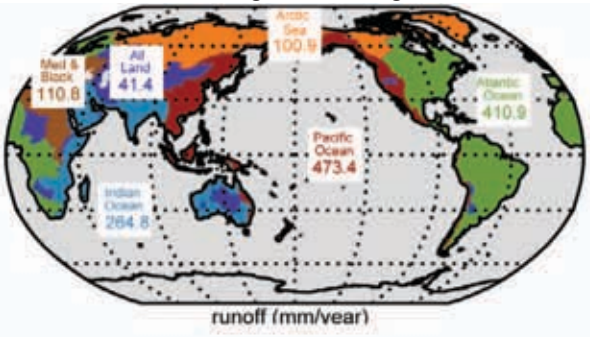

Sea Level Pressure

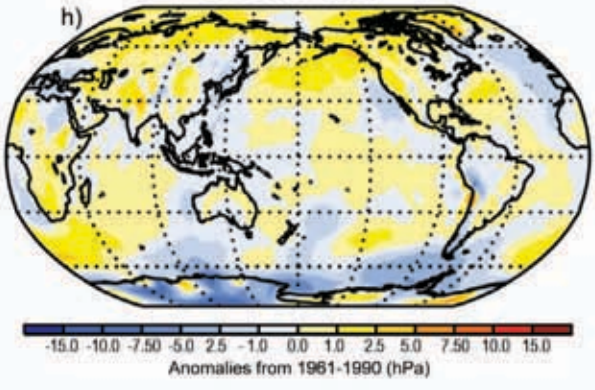

Surface Winds

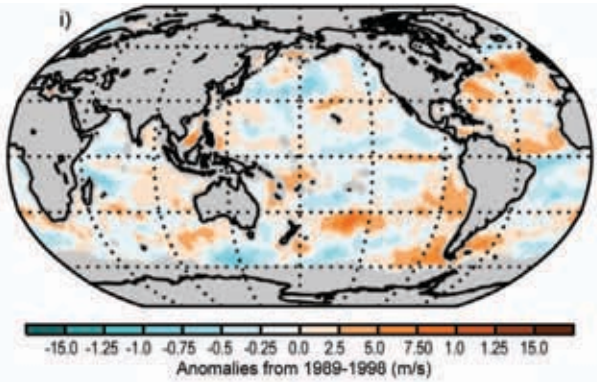

Ozone

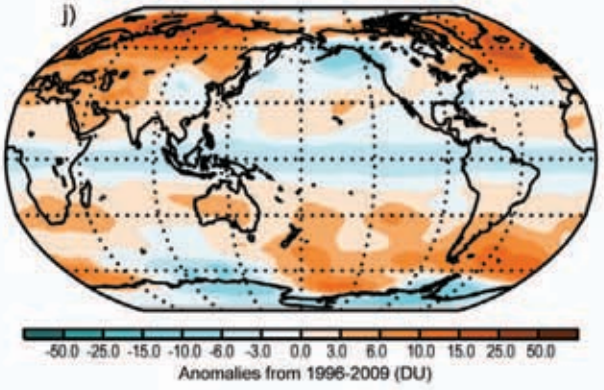

Fraction of Absorbed Photosynthetically Active Radiation

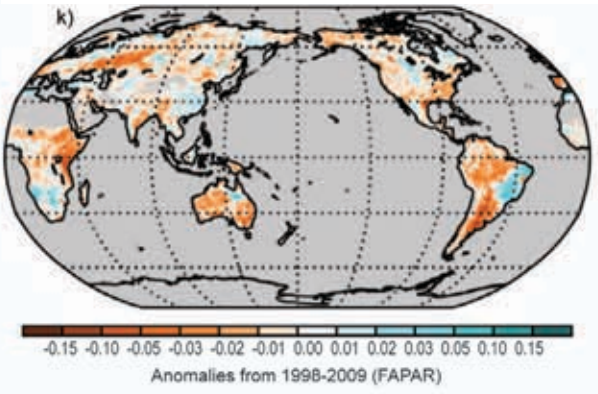

Biomass Burning (average fire radiative power)

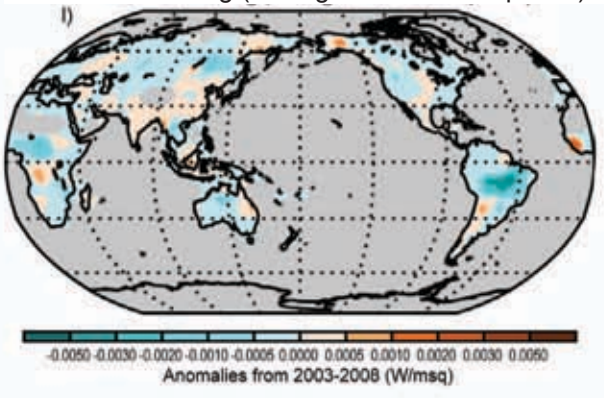

Table 2.1. Sources of those datasets used in this chapter that are publicly available for bona fide research purposes.

Source	Datasets	Section
http://www.metoffice.gov.uk/hadobs	HadCRUT3, HadAT2, HadCRUH, HadSLP2r	2b.2; 2b.3; 2b.4; sidebar 1; 2d.1
http://data.giss.nasa.gov/gistemp	GISS surface temperature record	2b.2; sidebar1
http://www.ncdc.noaa.gov/cmb-faq/anomalies.html	NOAA/NCDC surface temperature record	2b.2; sidebar1
http://www.ecmwf.int/research/era/do/get/index	ERA reanalysis products	2b (all sections)
http://www.remss.com	Remote Sensing Systems products MSU, SSM/I, TMI, AMSR-E	2b.3; 2b.4; 2c.1; 2c.2; 2d.2; sidebar1
http://vortex.nsstc.uah.edu/public/msu/	UAH MSU records	2b.3; 2b.4; sidebar1
http://www.ncdc.noaa.gov/oa/climate/ratpac	RATPAC	2b.3; 2b.4; sidebar1
http://www.univie.ac.at/theoret-met/research	RAOBCORE 1.4, RICH	2b.3; 2b.4; sidebar1
http://www.ccrc.unsw.edu.au/staff/profiles/sherwood/rad-proj/index.html	IUK	2b.4; sidebar1
http://www.star.nesdis.noaa.gov/smcd/emb/mscat/mscat-main.htm	STAR	2b.4; sidebar1
By email to Junhong Wang	GPS-PW	2c.1
http://cosmic-io.cosmic.ucar.edu/cdaac/index.html	COSMIC	2c.1; sidebar2
http://www.ncdc.noaa.gov/oa/climate/ghcn-monthly/index.php	GHCN data (T, precipitation)	2b.2; 2c.2
http://precip.gsfc.nasa.gov	GPCP precipitation	2c.2
http://www.cpc.noaa.gov/products/global_precip/html/wpage.cmap.html	CMAP precipitation	2c.2
http://www.esrl.noaa.gov/psd/data/gridded/data.gpcc.html	GPCC precipitation	2c.2
http://climate.rutgers.edu/snowcover	Snowcover extent	2c.3
http://www.atmos.washington.edu/~ignatius/CloudMap	SOBS clouds	2c.4
http://isccp.giss.nasa.gov	ISCCP D2 clouds	2c.4
http://cimss.ssec.wisc.edu/patmosx	PATMOS-x	2c.4
http://ladsweb.nascom.nasa.gov	MODIS	2c.4
http://eosweb.larc.nasa.gov/PRODOCS/misr/level3/overview.html	MISR	2c.4
http://grdc.bafg.de http://www.gtn-h.net	Global Runoff Data Centre Global Terriestrial Network for Hydrology	2c.5

Source	Datasets	Section
http://www.pecad.fas.usda.gov/cropexplorer/global_reservoir/index.cfm http://tethys.eaprs.cse.dmu.ac.uk/RiverLake/shared/main http://www.legos.obs-mip.fr/soa/hydrologie/hydroweb/ http://gcmd.nasa.gov/records/GCMD_GLWD.html	Lake level products	2c.6
http://www.bom.gov.au/climate/current/soi2.shtml	BoM SOI	2d.1
http://www.cpc.noaa.gov/products/precip/CWlink/daily_ao_index/ao_index.html	AO index	2d.1
http://manati.orbit.nesdis.noaa.gov/quikscat/	QuikScat	2d.2
http://science.larc.nasa.gov/ceres/	CERES data	2e
http://www.esrl.noaa.gov/gmd/ccgg/trends/	CO_2	2f.1i
http://www.cmdl.noaa.gov/odgi/	ODGI	2f.1ii
http://www.esrl.noaa.gov/gmd/aggi/	AGGI	2f.1iii
http://www.esrl.noaa.gov/gmd/hats/insitu/cats/cats_conc.html	Trace gas measures	2f.1iv
http://www.gmes-atmosphere.eu/	MACC/GEMS	2f.2; 2g.3
http://www.ndacc.org/data/data_tbl http://acdb-ext.gsfc.nasa.gov/Data_services/merged/ http://eosweb.larc.nasa.gov http://haloe.gats-inc.com http://eopi.esa.int/registration http://www.iup.uni-bremen.de/scia-arc/	Stratospheric ozone	2f.3
http://www.woudc.org/data_e.html http://acdb-ext.gsfc.nasa.gov/Data_services/merged/ http://www.iup.uni-bremen.de/gome/wfdoas/wfdoas.html	Total ozone	2f.3
http://www.geo.unizh.ch/wgms/	WGMS	2g.1
http://fapar.jrc.ec.europa.eu/	FAPAR	2g.2

cal Agency, and NCEP (CFFSR, Saha et al. 2010) and others as they complete and that these reanalyses can be incorporated for additional variables where deemed appropriate by the section authors.

2) Global surface temperatures—M. J. Menne and J. J. Kennedy

Global surface temperatures in 2009 saw a return to near-record levels as the cooling in the tropical Pacific associated with the 2007/08 La Niña event gave way to strengthening El Niño conditions in 2009 (Fig. 2.1). This led to large areas of the tropics experiencing higher-than-average temperatures towards the end of the year. According to the three major surface temperature datasets (Fig. 2.2, NASA/GISS, Hansen et al. 2001; HadCRUT3, Brohan et al. 2006; and NOAA/NCDC; Smith and Reynolds 2005, Smith et al. 2008) 2009 averaged about 0.1°C warmer than 2008, which was the coolest year since 2000. Anomalies from the 1961–90 average for 2009 were 0.50°C, 0.44°C, and 0.46°C, respectively, and 0.37°C, 0.31°C, and 0.38°C for 2008. Analyses are based on air temperature data over land and SSTs derived from ship and buoy reports with independently derived adjustments to account for changes in observing-system bias.

The three institutions use different reconstruction and interpolation techniques (Table 2.2), hence the analyses differ in some details, especially in data sparse regions and in the specifics of yearly rankings.

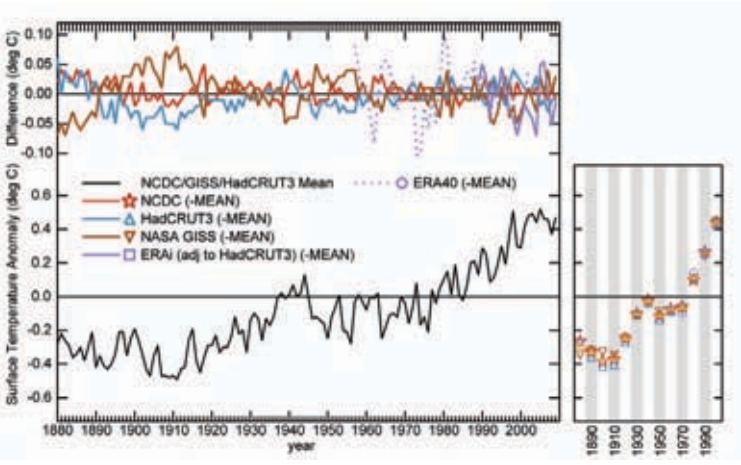

Fig. 2.2. Global surface temperature anomalies with respect to the 1961 to 1990 average: (bottom) mean of the NASA/GISS, HadCRUT3 and NOAA/NCDC analyses; (top) difference between NASA/GISS, HadCRUT3, NOAA/NCDC, ERA-interim, ERA-40 and the mean. Decadally averaged anomalies are shown on the right-hand side where 66% of months are present along with the multi-dataset mean. ERA-interim anomalies are with respect to a 1989–2008 climatology and so have been adjusted by the difference between the ERA-interim and HadCRUT3 mean over the 1989–1998 period for consistency. Documented issues exist with ERA-40 pre-1979, especially in the Southern Hemisphere and Antarctic (e.g., Simmons et al. 2004). ECMWF always tell users to use caution when mixing pre-1979 data from ERA-40 into a climate analysis.

Nevertheless, the three reconstructions are in close agreement regarding the low-frequency variations in the surface temperature signal as indicated in Fig. 2.2. Higher values in the NASA/GISS analysis in recent years may be a consequence of the Hansen et al. (2001) approach to interpolating and averaging temperature anomalies across the data sparse high Arctic where positive anomalies have been particularly large during the last few years. The tendency for much above-average temperatures in the high-latitude regions of the Northern Hemisphere continued in 2009 (Plate 2.1). Above average temperatures were also prevalent across much of Europe and Asia, Mexico, Africa, and Australia whereas cooler-than-average conditions occurred across the southern oceans, central Siberia, and the region spanning southern Canada and the north central contiguous United States.

Unusual warmth was widespread throughout the year. Southern Asia and north Africa were exceptionally warm in all seasons, in contrast the northern

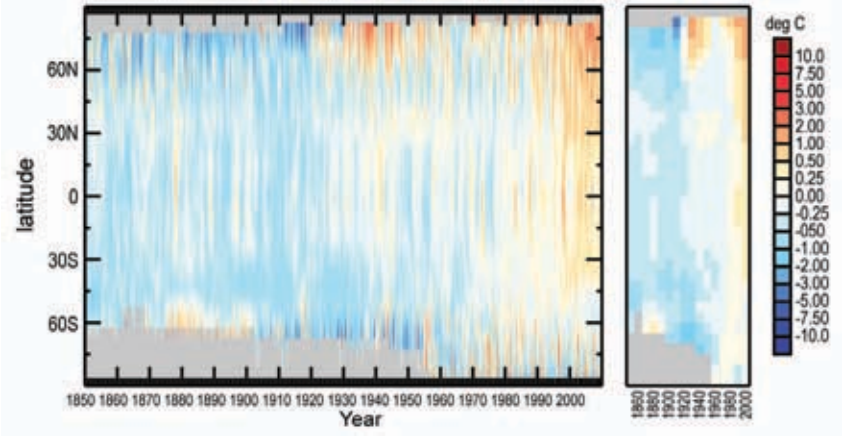

Fig. 2.1. HadCRUT3 monthly average temperature anomalies by latitude for the period 1850 to 2009. Decadally averaged anomalies are shown on the right-hand side where 66% of months are present. Grey areas indicate missing data. HadCRUT3 data have been smoothed in space and time using a 121 filter.

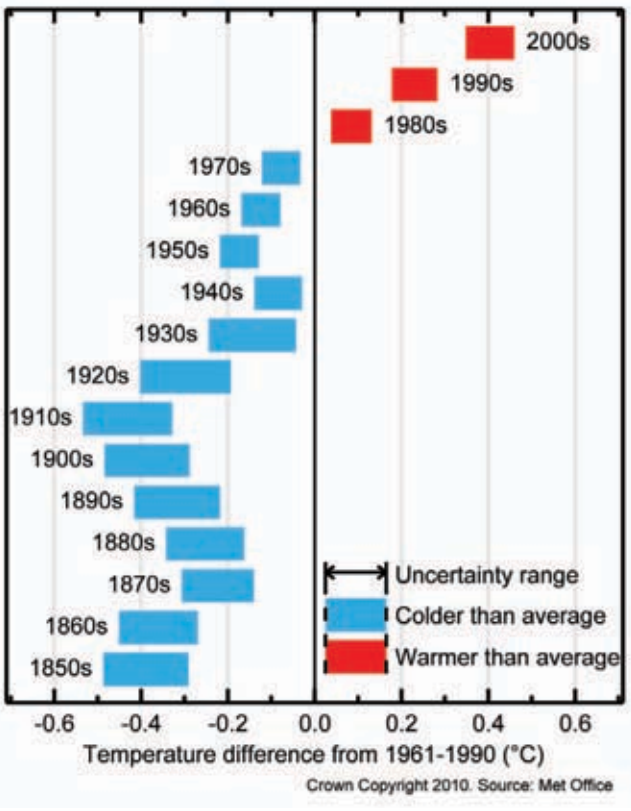

Fig. 2.3. 95% confidence range of decadal average temperatures for the HadCRUT3 temperature analysis (see Brohan et al. 2006 for the error model derivation).

U.S. and Canada were cooler than average for much of the year. In mid-December 2009 the Arctic Oscillation index turned strongly negative setting a pattern of colder-than-average temperatures over northern Eurasia and the U.S., coupled with warmer-than-average temperatures over the polar regions, southern Eurasia, and Canada that persisted throughout the winter. Nevertheless, December 2009 (and the rest of the winter season) was well above average in the North Hemisphere despite headlines about the unusual cold and snowy winter.

The uncertainties in deriving the global mean surface temperature imply that 2009 is statistically indistinguishable from the other high-ranking years shown in Fig. 2.2. Year to year variability is dominated by natural variability such as ENSO, but the effects of external climate forcings are expected to manifest themselves at decadal and longer time scales (Alley et al. 2007). Each of the last three decades was warmer than all earlier decades in the instrumental record (Fig. 2.3) and each set a new and statistically significant record, culminating in the 2000s, which was the warmest decade of all.

3) Lower tropospheric temperatures—J. Christy, M. Free, C. Mears, and L. Haimberger

The 2009 global average temperature of the lower tropospheric layer (TLT, surface to ~8 km, see Fig. 2.2 in Karl et al. 2006) was approximately +0.3°C above the 1979–98 average. The first half of the year was near the decade's average but the troposphere subsequently warmed quickly in response to the developing warm phase of ENSO (Fig. 2.4). When the tropical Pacific ocean experiences these large temperature anomalies, the atmosphere above responds with similar temperature changes which, for the global average, lag the surface fluctuations by two to four months (Christy and McNider 1994). In the 31 (satellite) and 52 (radiosonde) years of records, 2009 ranked as the sixth or seventh warmest (depending upon the choice of dataset) in the lower troposphere, being around 0.2°C to 0.3°C cooler than the warmest (El Niño) year of 1998. Areas in the Northern Hemisphere midlatitudes, including central North America, north Atlantic, northern Asia, along with the Antarctic Peninsula were below the base-period average. North polar regions, south Asia, Atlantic–Indian ocean basin, and much of the tropics were on average warmer than the mean (Plate 2.1).

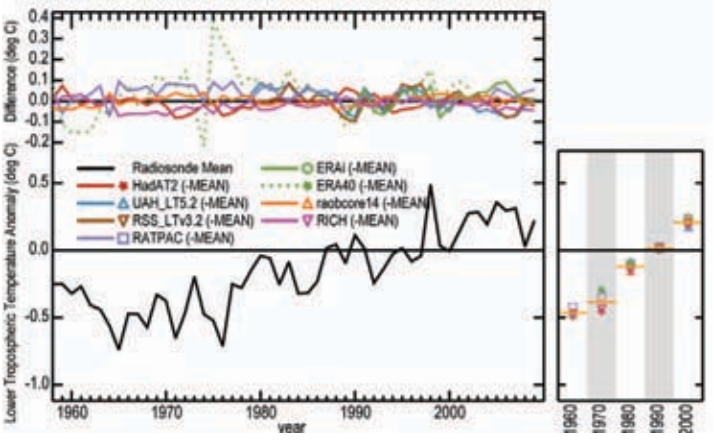

Fig. 2.4. As for Fig. 2.2 for global mean lower tropospheric temperature (1958–2009) from multiple datasets including four radiosonde datasets [HadAT2 (Thorne et al. 2005), RATPAC (Free et al. 2005), RAOBCORE and RICH (both Haimberger et al. 2008)], two satellite MSU datasets [UAH (Christy et al. 2003), RSS (Mears and Wentz 2009a)], and ERA-interim and ERA-40 Reanalyses (Simmons et al. 2010). Continuing research has documented procedures to account for inhomogeneities in these systems in order to provide the most confident estimates of the temperature values through time.

HOW DO WE KNOW THE WORLD HAS WARMED?—J. J. Kennedy, P. W. Thorne, T. C. Peterson, R. A. Ruedy, P. A. Stott, D. E. Parker, S. A. Good, H. A. Titchner, and K. M. Willett

Although the IPCC AR4 concluded that "warming of the climate system is unequivocal," public debate over the evidence for global warming continues. However, it is often confined to a small set of reiterated disputes about Land Surface Air Temperature (LSAT) records, diverting attention from the broader evidence basis.

The methods used to derive the principal estimates of global surface temperature trends—HadCRUT3 (Brohan et al. 2006), NOAA (Smith et al. 2008), and NASA/GISS (Hansen et al. 2001)—are largely independent (Table 2.2). So, the spread of the three estimates indicates the likely degree of uncertainty in the evolution of the global mean surface temperature. It is noteworthy that independently-derived estimates of tropospheric temperature trends for the whole troposphere channel (distinct from section 2b2) from satellites differ by an order of magnitude more than do estimated surface temperature trends (Thorne et al. 2010, manuscript submitted to *Wiley Interdisciplinary Reviews: Climate Change*).

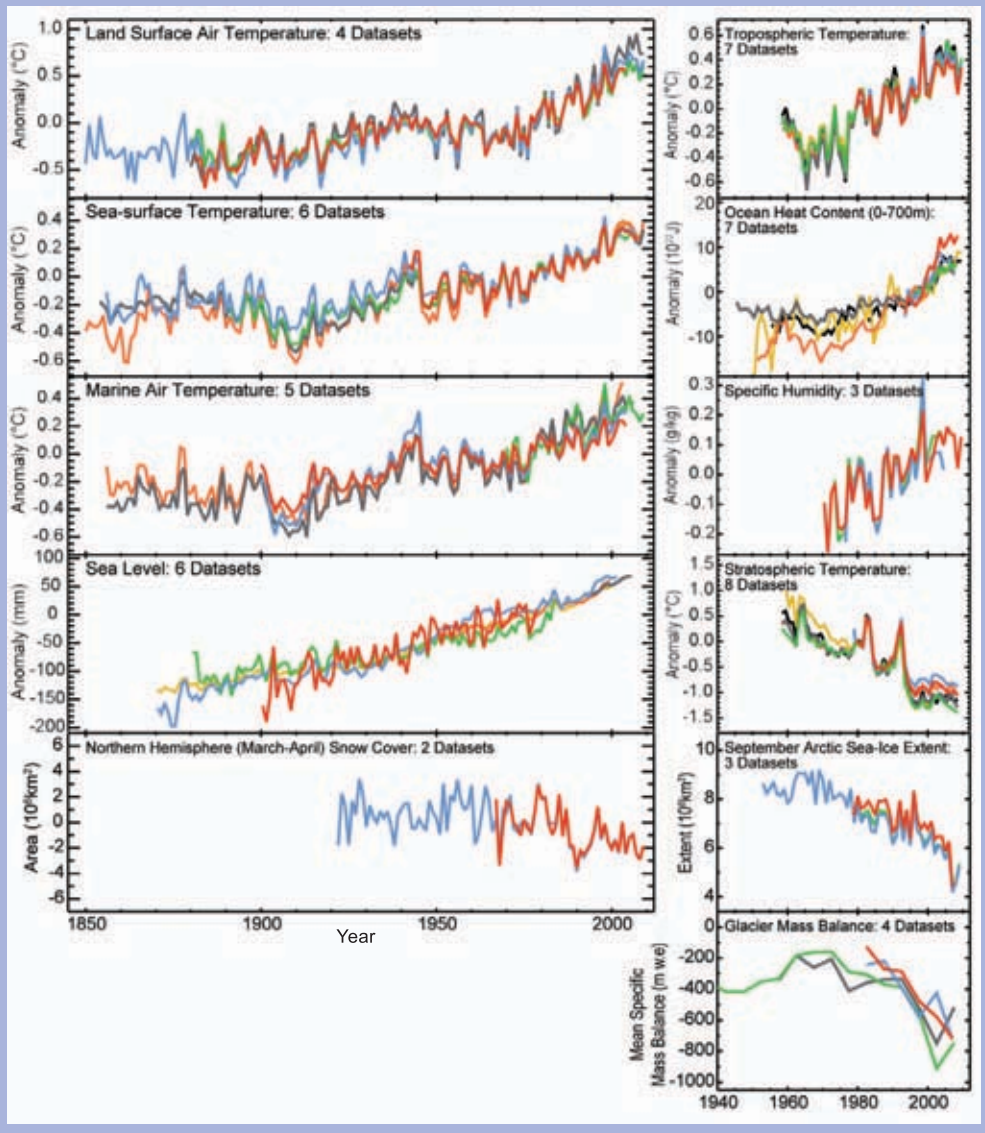

Fig. 2.5. Time series from a range of indicators that would be expected to correlate strongly with the surface record. Note that stratospheric cooling is an expected consequence of greenhouse gas increases. A version of this figure with full references is available at www.ncdc.noaa.gov/bams-state-of-the-climate/.

Numerous studies attest to the robustness of the global LSAT records and their nonreliance on individual stations (e.g., Jones et al. 1997; Peterson et al. 1999; Parker 2006; Parker et al. 2009; Menne et al. 2010). Evidence from recent reanalyses lends further support (Simmons et al. 2010).

The IPCC conclusion (Alley et al. 2007) that "warming of the climate system is unequivocal" does not rest solely upon LSAT records. These constitute only one line of evidence among many, for example: uptake of heat by the oceans, melting of land ice such as glaciers, the associated rise in sea level, and increased atmospheric surface humidity (Fig. 2.5). If the land surface records were systematically flawed and the globe had not really warmed, then it would be almost impossible to explain the concurrent changes in this wide range of indicators produced by many independent groups. The observed changes in a broad range of indicators provide a self-consistent story of a warming world.

Table 2.2. Comparison between the HadCRUT, NOAA and NASA/GISS global surface temperature analyses.

	HadCRUT	NOAA	NASA
Land Surface Air Temperature			
Number of station	c. 4500	4,400	c. 6300
Sources of station data	The CRU archive containing: GHCN (over 30 sources of data, most are not regularly updated), Antarctic SCAR (Scientific Committee on Antarctic Research) data, various regional compilations,paper archives, USHCN data. Regular updates primarily from-CLIMAT messages.	GHCN. Regular updates are primarily from USHCN data in the U.S. and CLIMAT messages.	GHCN, USHCN v2 adjusted, Antarctic SCAR (Scientific Committee on Antarctic Research) data.
Quality control (QC) procedures	Manual inspection; regional studies as published	Automatic QC tests based on statistics and physics (e.g., outlier tests, sequences of identical values).	Unrealistic outliers and segments of station series were eliminated after manual inspection.
Homogeneity adjustments	Visual and near-neighbor comparisons. c.20% of stations affected. Regional studies as published.	Non-climatic step changes and trends identified using USHCN v1 methods (US) and PEEP (Peterson and Easterling, 1994; Easterling and Peterson 1995) methods (remainder globe). Data adjusted to remove those artificial biases.	If there are multiple records at a given location, these are combined into one record adjusting according to the average difference during the period of overlap.
Urbanization effects	Some urban sites eliminated or adjusted by the QC and homogeneity adjustments. Uncertainty model includes a one-tailed urbanization error	Addressed by the homogeneity adjustments methodology.	Non-rural stations (defined by night-lighting in USA and by population data elsewhere) adjusted to match neighboring rural stations. Urban stations without nearby rural stations are dropped.
Ocean data			
Sources of station data	Ships, buoys from ICOADS (1850-1997) and GTS (1998 on)	Ships and buoys observations from ICOADS with updates from GTS.	HadISST1: 1870-1981. Reynolds et al. 2002: 11/1981-present
Quality control	Automatic QC tests based on statistics and physics (e.g. climatology-based outlier test, check against near neighbors)	Climatology-based removal of outliers.	HadISST1 and Reynolds are interpolated analyses with implicit QC so no GISS QC is applied.
Homogeneity adjustments	Physically based adjustments for changing types of buckets used to sample water in early 20th Century.	Statistical adjustment for the transition between buckets and engine intakes based on a relationship between SSTs and night time air temperature and global metadata for the timing of the transition.	HadISST1 and Reynolds are interpolated pre-adjusted analyses so no GISS specific homogeneity adjustment is applied.
Spatial interpolation, merging and calculating of global average			
Merging procedures	Land and ocean grid boxes merged with a weighting based on inverse error estimates for land and ocean data.	Land and ocean grid boxes with data merged with a weighting based on fraction of the grid box having land versus ocean.	After gridding, non-missing values are averaged over the zones 90°S-23.6°S,23.6°S-0,0-23.6°N,23.6°N-90°N; and the four means are averaged with 3:2:2:3 weighting to represent their area.
Accounting for data void regions	No infilling performed. Incomplete sampling accounted for in the uncertainty model.	Low frequency component filtered using very large grid boxes. Anomaly spatial covariance patterns guide interpolation of the high frequency component. Data sampling criteria limit how far interpolation can be made. Land and ocean data interpolated separately. Areas of sea ice are set to missing.	For each of 8000 equal area grid boxes, stations within that box or within 1200 km of the box centre are combined using the reference station method.
Calculation of global average	Average of gridbox area-weighted NH and SH values. Avoids over-weighting better sampled NH.	Area weighted analysis based on 5x5 degree grid boxes.	After gridding, non-missing values are averaged over the zones 90°S–23.6S, 23.6°S–0°, 0°–23.6°N, 23.6°N–90°N; and the four means are averaged with 3:2:2:3 weighting to represent their area.
Notes	The uncertainty model also takes into account incorrect/missing adjustments and temporal/measurement sampling errors.	The above was based on GHCN version 3 which is scheduled to be released in the spring of 2010.	Info from Hansen et al. 1999, 2001; and http://data.giss.nasa.gov/gistemp/ Code to calculate GISSTEMP is available from http://data.giss.nasa.gov/gistemp/sources/.

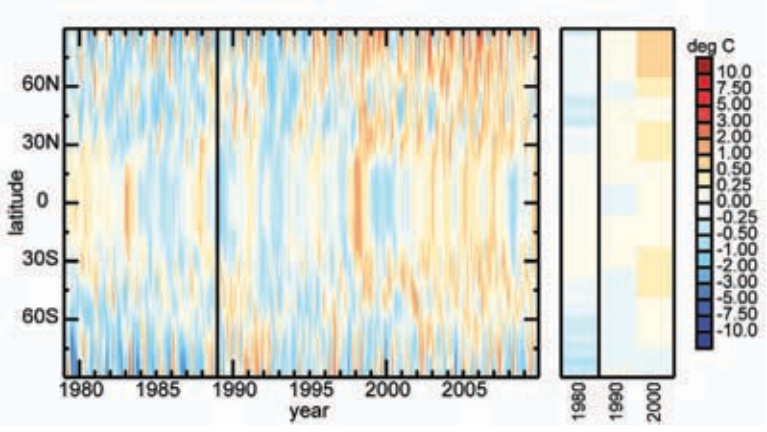

Fig. 2.6. As for Fig. 2.1 but for lower tropospheric temperature from the combined ERA-40 (1957 to 1988) and ERA-Interim (1989 to 2009) Reanalyses relative to the 1989 to 1998 base period.

The calendar decade of 2000–09 was the warmest of the last five decades. "Cool" La Niña conditions, persistent from late 1999, were evident as the decade began and reappeared in 2008. "Warm" El Niño conditions in 2003, 2005, briefly in 2007, and in the second half of 2009 were of modest magnitude compared with the significant event of 1997/98. Decades 1960–69 and 1970–79, were cooler than 2000–09 by about 0.6°C, with 1980–89 cooler by about 0.35°C and 1990–99 cooler by 0.2°C. The overall trend for both radiosondes (since 1958) and satellites (since 1979) is approximately +0.15°C per decade. Empirically the 52-year time series (Fig. 2.4) may equally plausibly be divided into three periods of relative temperature stability with transitions to warmer temperatures in 1977 (about +0.35°C) and 1998 (about +0.32°C) (e.g., Seidel and Lanzante 2004).

ECMWF Reanalyses (ERA-40 and ERA-interim) show that the warmest anomalies of 2000-09 were in the mid- and especially high-latitudes of the Northern Hemisphere. Similar regions in the Southern Hemisphere were not significantly different from the late 20th century (Fig. 2.6 – N.B. Choice of dataset is immaterial to the depiction of the main features as they are shown in all datasets). The Reanalyses reproduce the El Niño (warm, e.g., 1982-3, 1997-8) and La Niña (cool, e.g., 1989, 2008-9) events throughout the record. One to two year cooling periods follow volcanic eruptions in 1963 (Agung), 1982 (El Chichon) and 1991 (Mt. Pinatubo). Note the general trend toward warmer temperatures in the northern extratropics and tropics over the entire time period.

4) Stratospheric temperatures—M. Free and W. Randel

The 2009 annual average temperature of the global lower stratosphere was similar to that of the previous 15 years (Fig. 2.7), ranking 7th to 10th coolest since 1979 according to the dataset. Globally-averaged, the recent temperatures were approximately 1.5°C cooler than estimates from the late 1950s–early 1960s, when the first systematic radiosonde measurements of the lower stratosphere began. The overall cooling trend is punctuated by transient warming from three large volcanic eruptions (section 2b3), and the time series of cooling appears as step changes after these volcanic events (Seidel and Lanzante 2004; Ramaswamy et al. 2006). The volcanic warming events are mainly evident in low latitudes (Fig. 2.8).

The overall behavior of lower stratospheric temperature (TLS) shows reasonable agreement between radiosonde and satellite datasets for the post-1978 satellite period, although there are differences in detail between independent analyses of the radiosonde and satellite data (with the satellite data showing slightly less cooling than radiosondes). For the presatellite era (1958–78), there is larger disagreement and more uncertainty in trends among the different radiosonde-based datasets. For the overall record 1958–2009, the global trend from the average of the datasets is -0.33 ± 0.07°C per decade. For 1979–2009, trends range from -0.57 to -0.30°C per decade; the mean trend for all datasets shown is -0.41°C per decade.

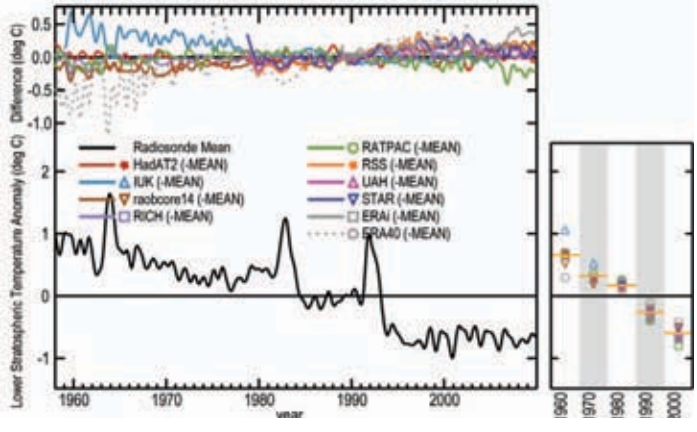

Fig. 2.7. As Fig. 2.2 but all time series are for the layer sampled by MSU channel 4 lower stratospheric temperature, spanning 10–25 km in altitude, with a peak near 18 km. References are the same as Figure 2.4 except for RSS (Mears and Wentz, 2009b) and the additional IUK radiosonde dataset (Sherwood et al. 2008) and STAR MSU record (Zou et al. 2009).

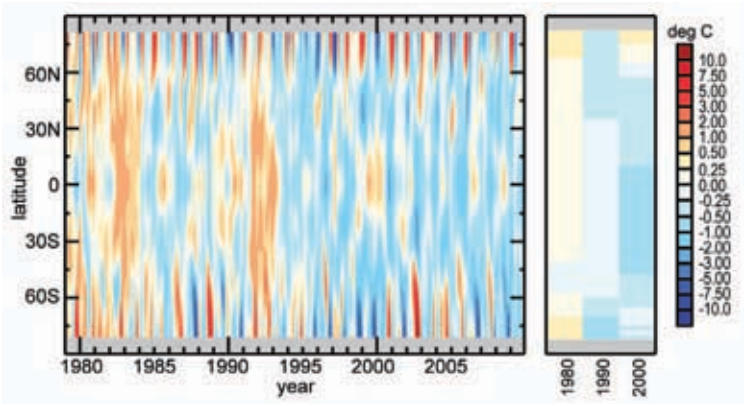

Fig. 2.8. As Fig. 2.1 but for the lower stratospheric channel estimate from RSS.

Evolution of lower stratospheric temperatures from satellite measurements (Fig. 2.8) highlights relatively constant temperatures since ~1995, modulated by the Quasi-Biennial Oscillation (QBO) in the tropics, plus large interannual variability in high-latitudes (during the respective winter–spring seasons). The QBO shifted from westerly to easterly winds in 2009, resulting in cold tropical lower stratosphere temperature anomalies in the second half of the year. The Arctic stratosphere was strongly influenced by a large stratospheric sudden warming in January 2009 (the largest in the 50-year record), resulting in rapid temperature increases of over 60°C in the polar middle and upper stratosphere (Fig. 2.9); the remainder of the Arctic winter (February–April) was relatively cold without large dynamic variability. The Antarctic polar vortex was relatively cold and undisturbed during 2009, with an ozone hole similar to other recent undisturbed years (Section 2f3).

TLS anomalies for 2009 (Plate 2.1) show large Arctic warming related to the January 2009 sudden stratospheric warming and a strong wave-1, or dipole pattern, in the zonal band around 60°S related to Antarctic changes in September–October. An increasing trend in this Antarctic pattern was noted in recent papers (Hu and Fu 2009; Lin et al. 2009).

As in previous years, changes in temperatures for altitudes above the lower stratosphere are difficult to characterize because of the relatively immature state of continuous datasets derived from the Stratospheric Sounding Unit (SSU), which ended in 2005, and the Advanced Microwave Sounding Unit (AMSU), with several different instruments operational since 1998.

c. Hydrological cycle

1) Total column water vapor—C. Mears, J. Wang, S. Ho, L. Zhang, and X. Zhou

Total column water vapor (TCWV) over the world's oceans has been monitored since the first Special Sensor Microwave/Imager (SSM/I) satellite in late 1987 (Wentz 1997). In this section, we use data from the SSM/I and the Advanced Microwave Scanning Radiometer Earth Observing System (AMSR-E) instruments. Independent evaluations have found these data to be accurate enough for climate studies (Trenberth et al. 2005). Beginning in the late 1990s, ground-based GPS measurements provide a second accurate measurement of TCWV (Wang et al. 2007). Since these stations are often land based, they provide an important complement to the ocean-only SSM/I measurements. Even more recently, the Constellation Observing System for Meteorology, Ionosphere and Climate (COSMIC, see sidebar) series of satellites have begun using satellite-to-satellite radio occultation (RO) measurements to make globally distributed measurements of water vapor profiles over land and ocean. Here COSMIC TCWV is calculated from corresponding water vapor profiles.

The map of TCWV anomalies (Plate 2.1) includes data both from SSM/I (over the oceans) and from a subset of the ground-based GPS stations with continuous data from 1997 to 2009. This subset was chosen so that a meaningful anomaly estimate can be calculated—many more stations would be avail-

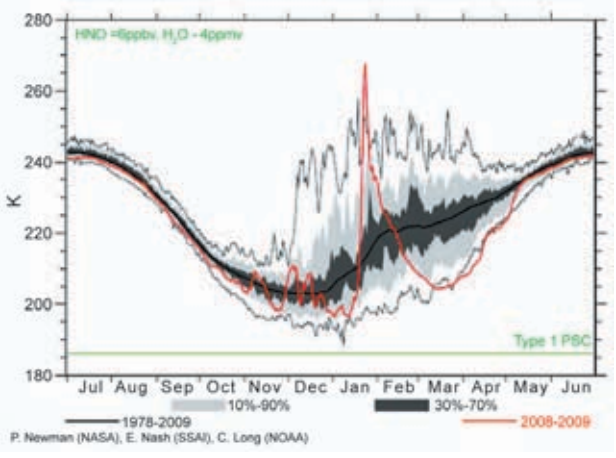

Fig. 2.9. Time series of 10 hPa temperature (red) at 80°N from CPC GFS analysis, highlighting January 2009 stratospheric sudden warming. Dark shaded areas indicate the range of the 30th to 70th percentile, light shade indicates the 10–90% range, and the light black lines indicate the maximum and minimum temperatures for the period since 1978.

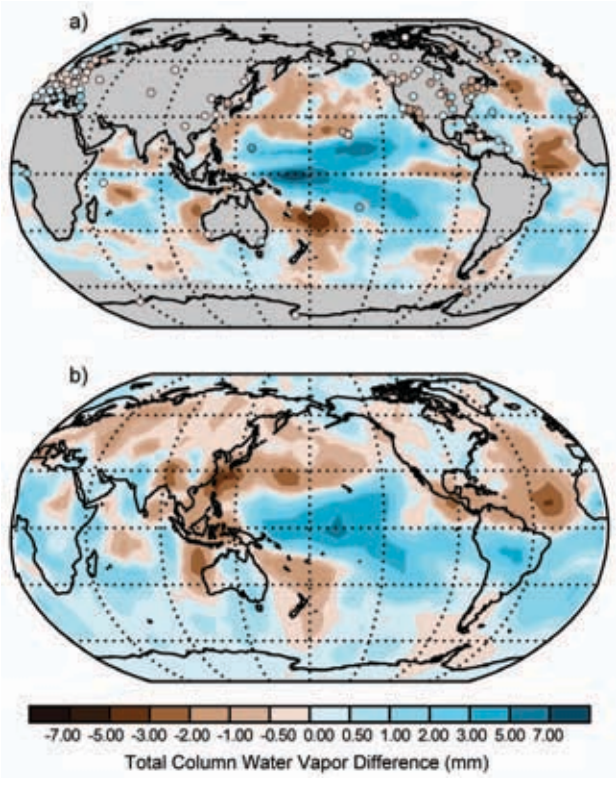

Fig. 2.10. Change in TCWV from 2008 to 2009. Panel (a) shows measurements from AMSR-E and ground based GPS stations, (b) from COSMIC.

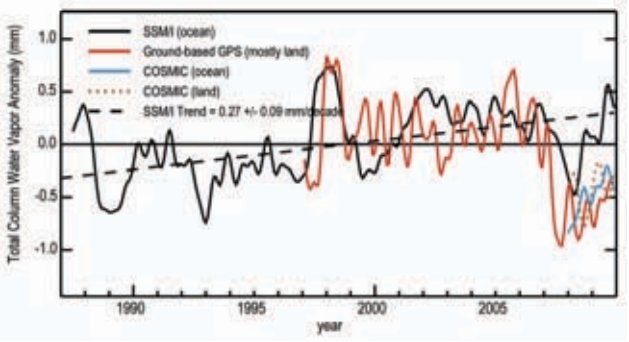

Fig. 2.11. Anomaly time series of TCWV both from SSM/I, ground based GPS, and COSMIC. Except for COSMIC, the reference period is 1997–2008. The COSMIC ocean anomalies are calculated relative to a SSM/I climatology for 1997–2008. The COSMIC land anomalies are calculated only at the locations of GPS ground stations, and are relative to a 1997–2008 ground-based GPS climatology. The timeseries have been smoothed to remove variability on time scales shorter than 6 months. A linear fit to the SSM/I data is also shown indicating an increasing trend in water vapor over the 1988–2009 period.

able if this requirement were relaxed since the size of the network is increasing rapidly with time. There is general agreement between the SSM/I and ground-based GPS measurements at locations where overlaps occur with differences typically less than 0.5 mm. In the latter half of the year, a large wet anomaly in the tropical Pacific was associated with the onset of El Niño conditions. In contrast, most regions outside the tropics were drier than normal.

Changes in TCWV from 2008 to 2009 measured by three different measurement systems show the dramatic moistening of the tropical Pacific as the climate system shifted from strong La Niña conditions in 2008 to moderate El Niño conditions by the end of 2009 (Fig. 2.10). The COSMIC measurements show this moistening extending across the Amazon basin, a region previously unobserved.

SSM/I TCWV, from the world's ice-free oceans, shows maxima in 1987/88, 1997/98, 2002, 2006/07, and 2009 (/10), associated with ENSO events, with GPS data, only available since 1997, showing similar features (Fig. 2.11). An exact match is not expected since the two measurement systems sample different regions of the globe. The COSMIC data show the sharp increase from 2008 to 2009 seen in the other two datasets. The SSM/I data show an increasing trend in TCWV (0.27 mm per decade). In the tropics this increase has been formally attributed to anthropogenic change over the 1988–2006 period (Santer et al. 2007). A Hoffmueller plot derived from SSM/I (Fig. 2.12) shows that the increase is largest in the tropics and Northern Hemisphere and relatively small in the Southern Hemisphere.

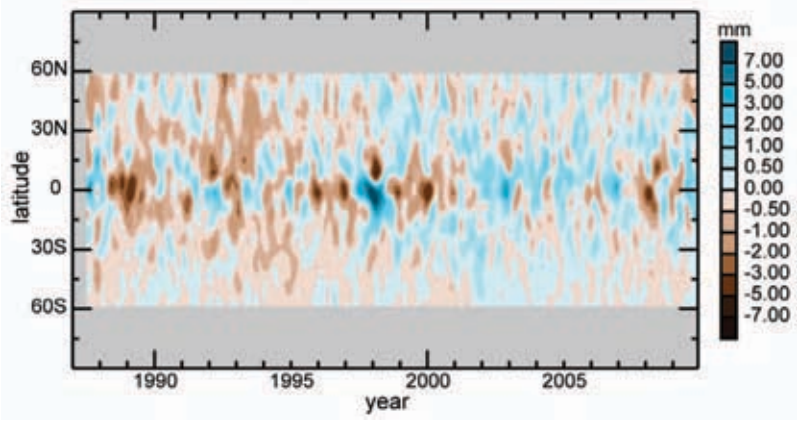

Fig. 2.12. As for Fig. 2.1 but for TCWV anomalies calculated using a reference period of 1988–2007. The data (SSM/I and AMSR-E measurements) have been smoothed in the time direction to remove variability on time scales shorter than 4 months.

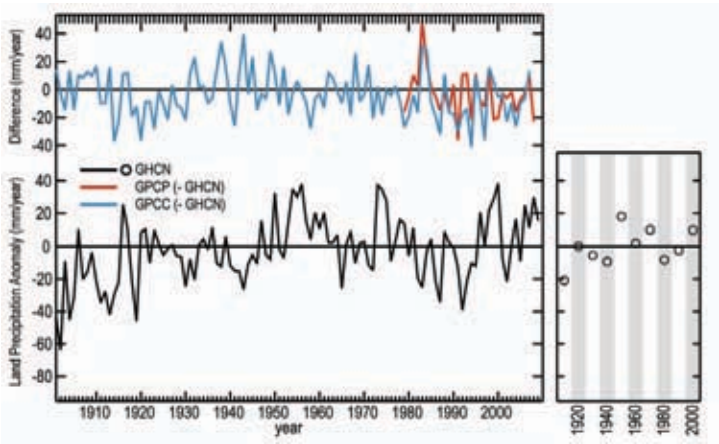

Fig. 2.13. As for Fig. 2.2 but for annual global land surface precipitation anomalies (mm) over the period 1901–2009 from the GHCN dataset relative to the 1961–1990 climatology (Vose et al. 1992). Two different historical comparisons of global land-based precipitation anomalies are also shown: beginning in 1901 using the difference between GPCC and GHCN, and beginning in 1979 using the difference between GPCP and GHCN (Schneider et al. 2008). All anomalies for the difference series were determined with respect to the 1981–2000 climatology.

2) Global precipitation—D. H. Levinson, K. A. Hilburn, J. H. Lawrimore, and M. C. Kruk

Global land precipitation estimates are derived from monthly totals of rain gauge measurements extending back at least to the beginning of the 20th century. In 2009 the positive anomaly continued an extended period of above average global precipitation covering the past five years (Fig. 2.13), and much of the period since 1996. Also shown (top curves) is the difference between global annual anomalies from three independent datasets (Global Historical Climatology Network [GHCN], Global Precipitation Climatology Centre [GPCC], and Global Precipitation Climatology Project [GPCP]). Overall, each of these datasets depict similar global anomalies on annual to interannual time scales, but some obvious differences occur on decadal timescales (e.g., during the early 1980s). Whether it is a gauge only (i.e., GHCN, GPCC) or a satellite-gauge blended product (i.e., GPCP), the gauge inventories used and the inclusion criteria applied to the analysis (i.e., percentage of data required during the base period), among other factors, lead to the observed differences in the annual anomalies over time.

Over the global oceans, precipitation records are only available for the much shorter satellite era. Remote Sensing Systems (RSS) produces inter-calibrated passive microwave rain retrievals; which include retrievals from a total of eight microwave imagers into monthly-averaged maps at 2.5° x 2.5° resolution. For 2009, this included retrievals from TMI on TRMM, AMSR-E on Aqua, and F13 SSM/I on DMSP until it stopped functioning in late November 2009. There is substantial disagreement among three satellite-derived precipitation products over the ocean: RSS (Hilburn and Wentz 2008), Version 2.1 GPCP (Adler et al. 2003), and CMAP (Xie and Arkin 1997), especially during the first half of the time period (Fig. 2.14). RSS and GPCP trends for 1988–2008 were similar (19.5 ± 7.7 mm year^{-1} decade^{-1} and 14.8 ± 9.1 mm year^{-1} decade^{-1}, respectively; Levinson et al. 2009), but there are notable differences between the new version of GPCP and that used last year. However, in both versions there has been a relative drift compared to RSS since 2005. Based on updated analysis (Fig. 2.14), their 1988–2009 trends differ significantly and now exceed the 95% confidence interval. The RSS trend has not changed much, currently at 20.4 ± 7.1 mm year^{-1} decade^{-1}, but the GPCP trend is much lower at 2.4 ± 8.1 mm year^{-1} decade^{-1}.

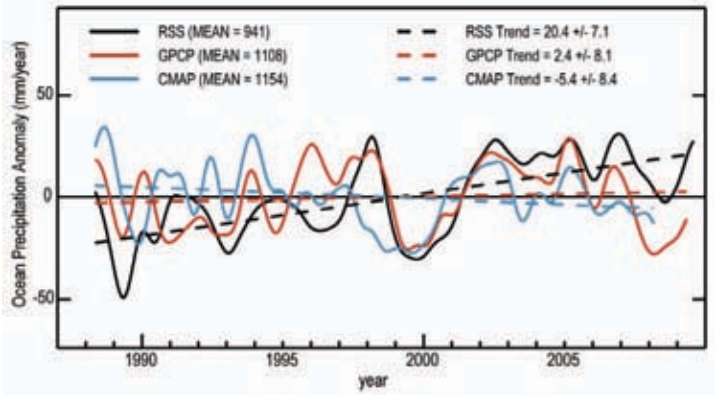

Fig. 2.14. Time series of precipitation anomalies relative to the period 1988–2009 for three datasets: RSS (black), GPCP (blue), and CMAP (red). Averages are for the global ocean equatorward of 60° latitude using a common definition of "ocean". The annual cycle has been removed and the time series have been low-pass filtered by convolution with a Gaussian distribution, with 4-month width at half-peak power. RSS data are available through all of 2009, GPCP data are available through September 2009, and CMAP data are available through July 2008. The key gives the 1988–2009 mean (in units of mm year^{-1}) and the linear trend (in units of mm year^{-1} decade^{-1}) with the 95% confidence interval. The linear trends are shown by the straight lines. The confidence interval is estimated based on deviations from the linear fit, and does not represent a particular dataset's "error".

Precipitation anomalies in 2009, over both land and ocean reflected the transition from La Niña at the end of 2008 to El Niño by late 2009. Over land, several regions experienced significant changes as a result. Long-term drought conditions in the southeastern United States persisted during the winter of 2008/09 (DJF; Fig. 2.15a), dissipated during the boreal spring (MAM; Fig. 2.15b), and were replaced by pronounced wet anomalies in the boreal fall as the El Niño developed (SON; Fig. 2.15d). Similarly, dry conditions that dominated northern Argentina for most of 2009 eventually broke later in the year as wet anomalies developed during the austral spring (SON; Fig. 2.15d). Abnormally dry conditions were also observed in southern Asia and the Indian subcontinent during the southwest monsoon (JJA; Fig. 2.15c).

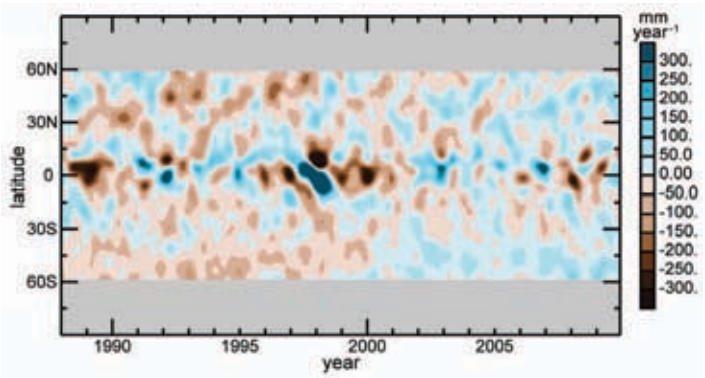

Fig. 2.16. As for Fig. 2.1 but for global ocean precipitation anomalies (with units of mm year^{-1}) as observed by the RSS monthly average dataset. The anomaly is calculated using the 1988–2009 base period by removing the latitude-dependent annual cycle.

During the La Niña in early 2009, a dry anomaly covered the western and central Pacific, with a wet anomaly over the far western Pacific Ocean. As the equatorial Pacific basin transitioned from La Niña to El Niño, dry anomalies over the western equatorial Pacific expanded, as wet anomalies in the far western Pacific region weakened (Plate 2.1). Dry conditions were also observed over parts of the central southern Pacific and Indian Ocean basins. The most pronounced precipitation signal over the oceans was a dry anomaly over the tropical Atlantic along the climatological latitude of the ITCZ just north of the equator. This was in conjunction with a weaker wet anomaly just south of the equator indicating an anomalous southward excursion of the ITCZ. Precipitation anomalies over the tropical oceans were relatively weak compared to other years (Fig. 2.16). In addition, the wetter-than-normal conditions over the Southern Ocean that started in 2000 continued through 2009.

3) Northern Hemisphere continental snow cover extent—D. A. Robinson

Annual snow cover extent (SCE) over the Northern Hemisphere (including snow over the continents and the Greenland ice sheet) was 0.4 million km^2 less than the 40-yr average; 2009 experienced the 13th least extensive cover on record (Table 2.3). The SCE in 2009 ranged from 47.1 million km^2 in January to 2.4 million km^2 in August.

2009 began with SCE in the second highest quartile over Eurasia and North America. North American extent remained within this quartile until April. However, Eurasian SCE fell into

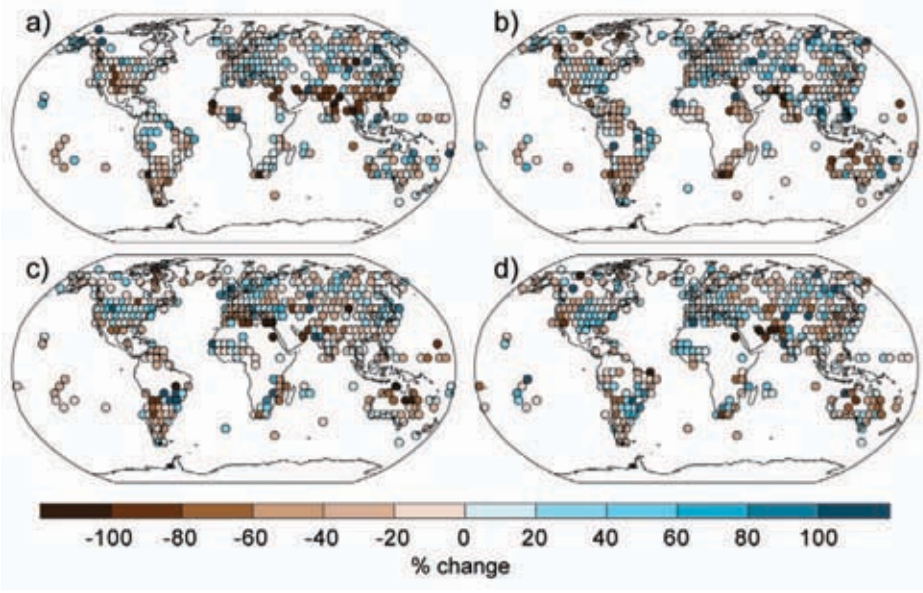

Fig. 2.15. Global precipitation anomalies (in % change) determined using the GHCN-Monthly dataset for the following 3-month seasons: (a) Dec 2008 to Feb 2009, (b) Mar to May 2009, (c) Jun to Aug 2009, and (d) Sep to Nov 2009. Seasonal anomalies were determined relative to the 1961–90 means, with at least two-thirds (66%) of the years without missing data required during the base period.

Table 2.3. Monthly and annual climatological information on Northern Hemisphere (NH) and continental snow extent between November 1966 and December 2009. The years 1968, 1969, and 1971 have 1, 5, and 3 missing months, respectively, so are not included in the annual (Ann) calculations. North America (N. Am.) includes Greenland. Ranks are from most extensive (1) to least (ranges from 40 to 44 depending on the month). (Source: Rutgers Global Snow Lab.)

	Number of years with data contributing to the record	Mean snow extent ($\times 10^6$ km^2)	Standard Deviation ($\times 10^6$ km^2)	2009 snow extent ($\times 10^6$ km^2)	2009 NH rank	Eurasia rank	N. Am. rank
Jan	43	46.6	1.5	47.1	14	17	16
Feb	43	45.5	1.8	44.5	34	35	16
Mar	43	40.3	1.9	39.3	29	35	20
Apr	43	30.6	1.7	29.2	33	40	12
May	43	19.6	1.7	18.0	37	38	22
Jun	42	10.2	2.0	7.1	41	41	38
Jul	40	4.2	1.2	2.7	39	40	38
Aug	41	3.1	0.7	2.4	37	39	32
Sep	41	5.3	0.9	4.3	34	38	23
Oct	42	17.9	2.6	20.7	6	10	3
Nov	44	33.6	2.0	34.4	14	5	41
Dec	44	43.2	1.8	45.9	2	7	1
Ann	40	25.0	0.9	24.6	28	29	19

the lowest quartile in February where it remained until early fall. Being the larger of the two continents, this most often placed the hemispheric landmass into the lowest quartile until fall. SCE increased rapidly across both continents in early October, with Eurasia maintaining a top 10 ranking throughout the remainder of the year. North American SCE flipped from third most extensive in October to fourth least extensive in November and then to the most extensive of the satellite era in December. This exemplifies the significant intra- and inter-seasonal variability of continental snow extent, particularly during the fall season. Hemispheric SCE in December was the second greatest of the past 44 years, doubtless linked to the extreme negative phase of the Arctic Oscillation and associated circulation anomalies (Fig. 2.29).

Late-year positive SCE anomalies resulted in the twelve-month running mean of Northern Hemisphere extent rising from its low extent of the past approximately two years and approaching the long-term mean (Fig. 2.17). Both hemispheric and Eurasian (Fig. 2.17) running means had not been as consistently low since the late 1980s and early 1990s. Meanwhile, the North American running mean remained close to the long-term mean throughout 2009.

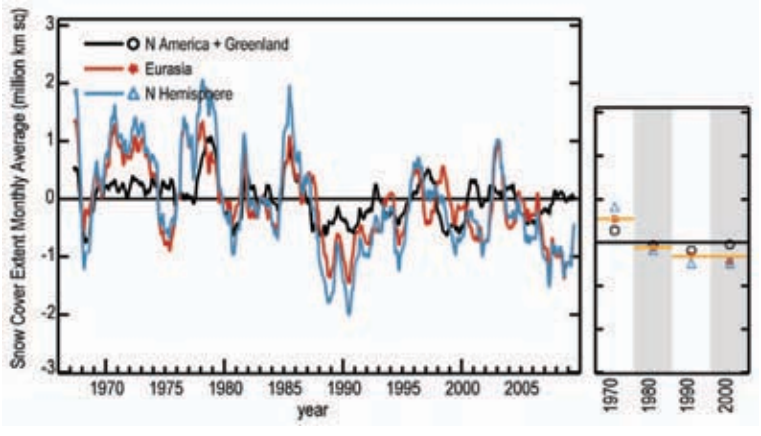

Fig. 2.17. As for Fig. 2.2 but for monthly anomalies of mean snow cover extent between November 1966 and December 2009 over Northern Hemisphere lands (including Greenland), Eurasia and N. America. Running monthly means are plotted on the seventh month of a given interval. Anomalies are calculated from NOAA snow maps. Mean hemispheric snow extent is 25.0 million km^2 for the full period of record. Monthly means for the period of record are used for nine missing months between 1968 and 1971 in order to create a continuous series of running means. Missing months fall between June and October, no winter months are missing.

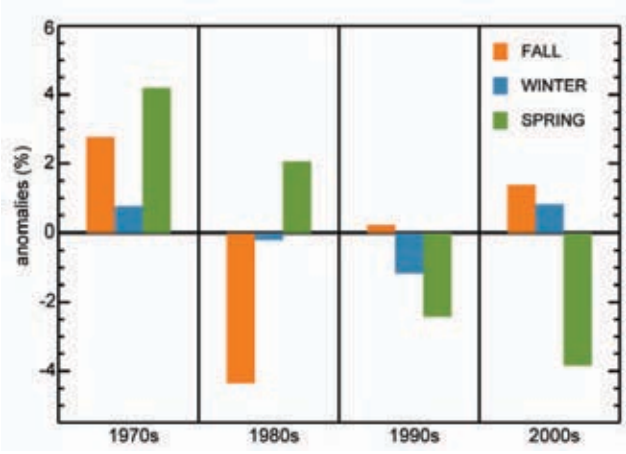

Fig. 2.18. Seasonal SCE anomalies (excluding summer) for the four decades beginning in December 1969 and ending in November 2009. Decadal percent anomalies are calculated for the 40-year interval.

Decadal snow cover extent behavior over Northern Hemisphere land regions between 1970 and 2009 was quite different between seasons (Fig. 2.18). The 1970s had the most extensive fall snow cover, with the 1980s the least extensive (approx -4% and the only decade below average). Winter SCE was almost equally above the 40-yr mean in the 1970s and 2000s, close to average in the 1980s, and below average in the 1990s. All winter decadal means were within 1.2% of average. Spring SCE steadily declined from the 1970s to 2000s, with these decades approximately +4% and -4% relative to the mean, respectively.

4) Global cloudiness—M. J. Foster, S. A. Ackerman, A. K. Heidinger, and B. C. Maddux

Global cloud anomalies in 2009 reflected the shift from weak La Niña conditions to an El Niño during boreal summer. The resulting temperature and circulation anomalies enhanced large-scale convection in the central Pacific and suppressed convection in the western Pacific near Indonesia. This generated positive cloud anomalies in the central equatorial Pacific and corresponding negative anomalies around Indonesia in the latter half of the year. Large positive annual anomalies of 10% to 15% were seen off the western coast of Peru and eastern coasts of Australia and Papua New Guinea (Plate 2.1). Since the shift to El Niño conditions did not occur until boreal summer, the magnitudes of the annual cloud anomalies were relatively small. Only small portions of the anomaly off the west coast of Peru were statistically significant at the 5% level. 2009 also saw some unusual continental cloudiness with positive cloud anomalies over large portions of northwestern Africa coupled with negative anomalies over eastern Africa (Plate 2.1), sustained throughout much of the year. Parts of Brazil also maintained positive cloud anomalies for much of 2009 and an interesting though short-lived cloudiness event occurred over the continental United States. Large positive anomalies over most of North America in October 2009 (Fig. 2.19) coincided with the wettest October since records began in 1894. Portions of the Midwest cloudiness anomalies are statistically significant at the 5% level.

Global mean monthly cloud anomalies from four different satellite cloud climatologies and surface observations (Fig. 2.20) are defined as each month minus its corresponding time series monthly mean. Differences in cloudiness estimates can in part be attributed to variations in how cloud-masking algorithms define cloud versus clear-sky thresholds. This is in addition to correcting for factors such as sensor viewing angle, pixel footprint size, spectral channels, diurnal satellite drift, and sensor calibration. The trend of cloud anomalies over the last four decades is smaller than seasonal and diurnal variability and within the range of estimated uncertainties for each product. With that in mind t-values are calculated for the slope of each month to remove seasonal effects: the surface weather observations (Fig. 2.20) data record shows a positive trend for all months while the International Satellite Cloud Climatology Project (ISCCP, Fig. 2.20) record shows a negative trend. None of the other records show significant trends. Relative to the entire Pathfinder Atmospheres Extended (PATMOS-x, Fig. 2.20) time series, 2009 was slightly cloudier-than-normal. The mean cloudiness for the year was 65.6%, 0.3% higher than the 28-year average, making 2009 the ninth cloudiest of the time

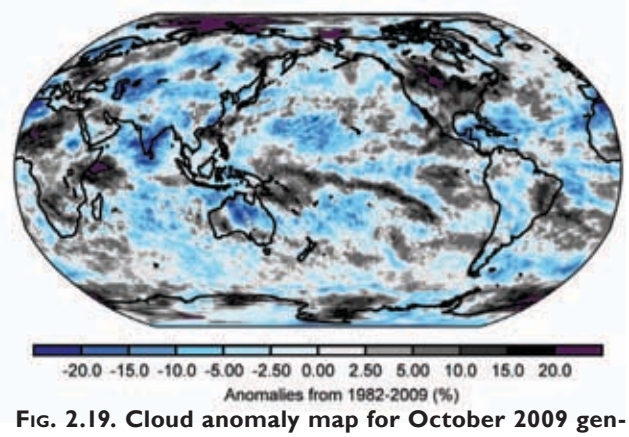

Fig. 2.19. Cloud anomaly map for October 2009 generated from the 28-year Pathfinder Atmospheres Extended (PATMOS-x, Heidinger and Pavolonis 2009) cloud climatology (1982 to present), which is derived from NOAA's Advanced Very High Resolution Radiometer (AVHRR).

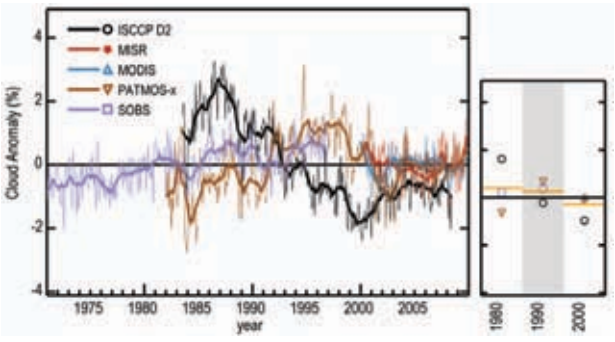

Fig. 2.20. As for Fig. 2.2 but for monthly anomalies of cloud amount from 1971 through 2009 taken from five datasets. Climatologies are derived from different instruments and cover different periods, the earliest of which are (a) surface weather observations (SOBS) from 1971 to 1996 (Hahn and Warren 2007); (b) Moderate Resolution Imaging Spectroradiometer (MODIS, Ackerman et al. 2008); (c) Multiangle Imaging Spectroradiometer (MISR, Di Girolamo et al. 2010) instruments on NASA's Terra satellite from 2000 to present (a MODIS instrument is also located on NASA's Aqua satellite and is included in the climatology); (d) International Satellite Cloud Climatology Project (ISCCP) data derived from imaging radiometers on operational weather satellites of several nations from 1983 to 2008 (and continuing); and (e) PATMOS-x described in Fig. 2.19. Thick solid lines represent average cloudiness for each dataset using a boxcar filter with a twelve-month window.

series. Nine months had higher cloudiness than the monthly mean (not significant), with only April, May, and August falling below the mean.

5) River discharge—B. M. Fekete, R. B. Lammers, A. MacDonald, L. C. Bowling, and R. Lawford

Discharge gauges are efficient and relatively inexpensive, and river discharge is the most accurately measured component of the water cycle (Fekete et al. 2002; Hagemann and Dümenil 1998). While modern telecommunication technologies are readily available to share in situ observations in a timely manner, the lack of international cooperation and data sharing are the main obstacles in accessing discharge data. For this reason historical runoff analyses are always delayed by three to five years and are incomplete in important geographical areas. As few as ~300 discharge gauges, strategically located near river mouths of large rivers around the world, could monitor over 50% of the continental land mass (Fekete et al. 2002). The World Meteorological Organization is proposing to establish 265 real-time reporting discharge gauges globally (to monitor 40% of the continental land mass) as the number of operating discharge gauges has steadily declined since the mid-1980s (Shiklomanov et al. 2002; Vörösmarty et al. 2002) at the same time as concerns about climate change effects are growing.

The only way to reconstruct recent changes in global runoff is to carry out water balance calculations using a relatively simple configuration of the Water Balance Model driven by observed air temperatures and precipitation (Vörösmarty et al. 1998; Wisser et al. 2008, 2010). Water balance calculations were carried out for the periods of 1901–2002, 1948–2007, 1986–2008, and 2003–05 using combinations of different climate forcings (due to the lack of single consistent time series from the beginning of the 20th Century to present). The overlapping periods were used to reconcile the different runoff estimates.

The reconciled runoff estimates (Fig. 2.21/Plate 2.1) reveal that the last decade (2000–09) had similar or increased river discharge in all continents and ocean catchments, except Africa and the Mediterranean/Black Sea drainage when compared to the long-term mean. 2009 appeared to return to the 20th Century global average except over Africa, the Pacific Islands, South America, and the Arctic and Pacific Oceans. Most of the continents show similar patterns except Africa, which is drying steadily and Asia, which fell below the 20th Century average in 2009.

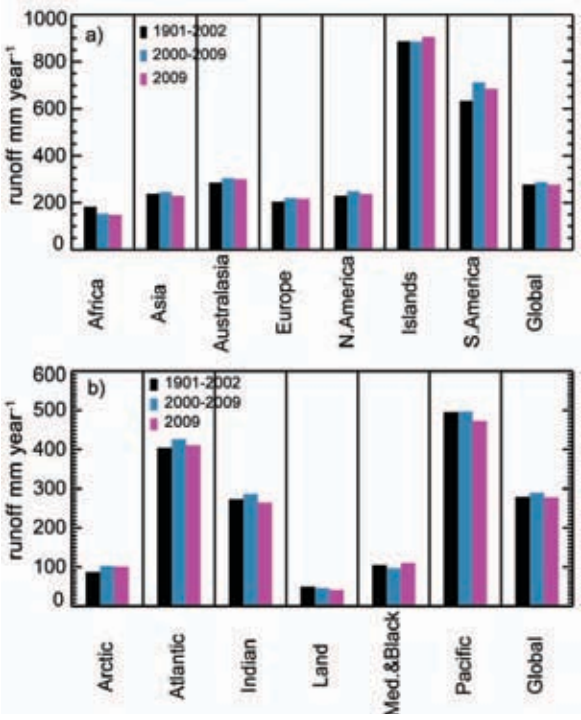

Fig. 2.21. River runoff by (a) continent and (b) receiving oceans. "Islands" refers to the Pacific Islands, "Med. & Black" refers to the Mediterranean and Black Sea drainage regions and "Land" represents the mean of all internal (endorheic) basins found on every continent.

USING SI-TRACABLE GLOBAL POSITIONING SYSTEM RADIO OCCULATION MEASUREMENTS FOR CLIMATE MONITORING—

S-P. HO, Y.-H. KUO, W. SCHREINER, AND X. ZHOU

Global Positioning System (GPS) Radio Occultation (RO) data are an important component of the evolving global observing system (NRC 2007; WMO 2007; GCOS 2004). GPS-RO is the only self-calibrated observing technique from space whereby its fundamental measurement is traceable to the international system of units (SI) (SI traceability; Ohring 2007). GPS receivers on low-Earth orbiting (LEO) satellites receive measurable radio frequency signals transmitted from GPS satellites; monitoring and corrections from a series of atomic clocks allows the signal timing to be traced to the SI second with a high degree of accuracy. Significant advantages of SI-traceable GPS-RO observations for climate monitoring include: (i) no satellite-to-satellite bias (Hajj et al. 2004; Ho et al. 2009a); (ii) great precision (Anthes et al. 2008; Foelsche et al. 2009; Ho et al. 2009a); and (iii) no synoptic sampling bias (cloud/precipitation effects).

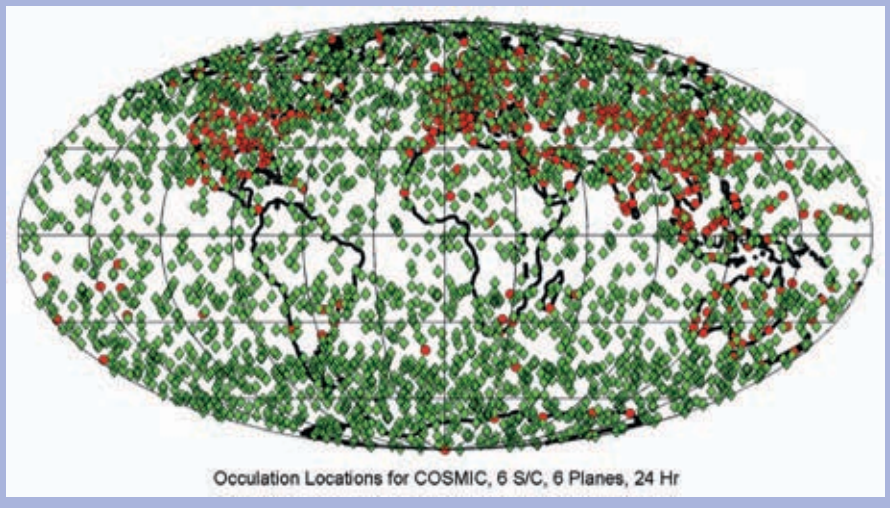

Fig. 2.22. Typical operational distribution of COSMIC GPS radio occultation soundings (green dots) over a 24-hr period across the globe. Red dots are locations of operational radiosonde stations.

Raw RO observations and precise positions and velocities of GPS and LEO satellites, can be used to derive atmospheric temperature and moisture profiles (Hajj et al. 2004; Kuo et al. 2004; Ho et al. 2009b). GPS-RO temperature can be validated by comparing temperature measurements from FORMOSAT-3/ COSMIC with high quality radiosonde measurements. With a uniform distribution of COSMIC RO data in time and space (~2500 profiles per day, Fig. 2.22), more than 10 000 collocations of Vaisala-RS92 radiosonde and COSMIC data within 2 hours and 300 km exist (Fig. 2.23). The precision of COSMIC derived temperature profiles is estimated to be better than 0.05 K from 8 km to 30 km (Ho et al. 2009a); COSMIC temperature is very close to radiosondes from 200 hPa to 20 hPa (around 12 km to 25 km). Because the quality of RO data does not vary with location and time, it is very useful for assessing systematic errors in different radiosonde sensors (e.g., He et al. 2009; Kuo et al. 2005; Elliott and Gaffen 1991; Luers and Eskridge 1998). Radiative temperature biases that vary during the day and night can be identified for different radiosonde sensor

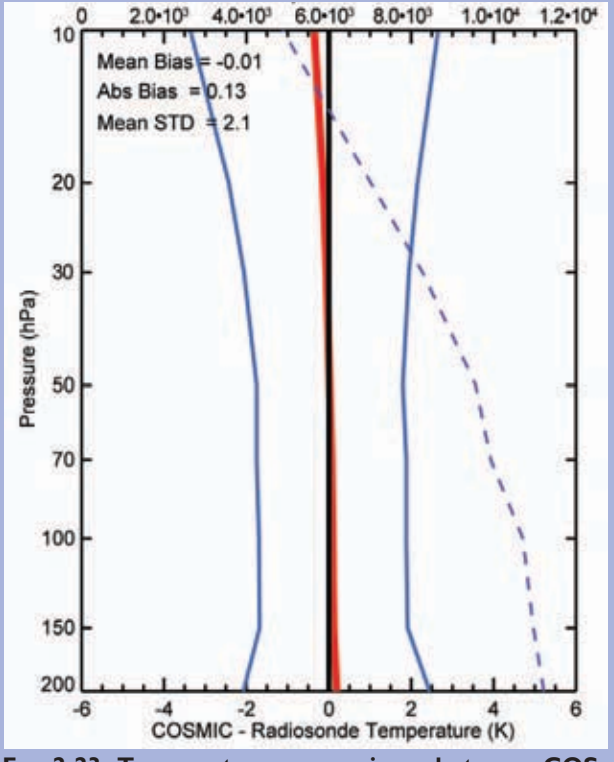

Fig. 2.23. Temperature comparisons between COSMIC and radiosonde Vaisala-RS92 in 2007. Mean bias, absolute mean bias and mean standard deviation are computed from 200 hPa to 10 hPa. The red line is the mean difference, the blue line is the standard deviation, and the dotted line is the sample number for RO and radiosonde pairs in that height (upper horizontal axis).

types when comparing with collocated COSMIC RO soundings (He et al. 2009).

The upper troposphere and lower stratosphere (UT/LS) is a critical region for understanding the radiative balance of the climate system and climate processes. However, due to poor vertical resolution and/or fundamental measurement uncertainty, most in situ and satellite sounder measurements of meteorological parameters in this region are not suitable for climate monitoring (Karl et al. 2006). The very high precision and vertical resolution (from ~60 m near the surface to ~1.5 km at 40 km) of GPS-RO data makes them very suitable to detect changes in UT/LS temperature (Ho et al. 2007), tropopause height, and the distribution of double tropopauses (Randel et al. 2007). Because GPS-RO data are not affected by on-orbit heating and cooling of satellite components, they are very useful for identifying the time/location dependent biases of microwave sounders (Ho et al. 2009c), making them potentially useful as a climate benchmark (Ho et al. 2009a) in addition to being well suited to detect climate trends (Ho et al. 2009b; Ringer and Healy 2008).

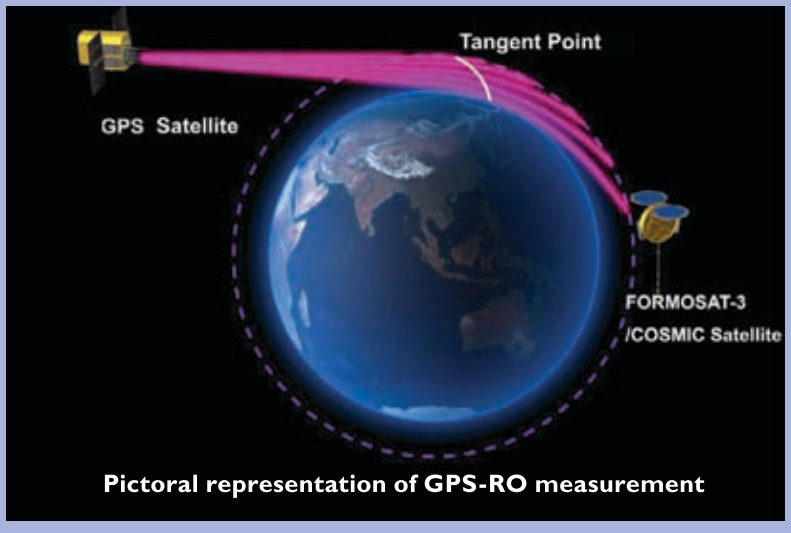

Pictoral representation of GPS-RO measurement

Using refractivity data and reasonably independent temperature profiles, highly precise COSMIC water vapor profiles can be derived. Comparisons of total-column water vapor (TCWV) from COSMIC with those derived from ground-based GPS (i.e., International Global Navigation Satellite Systems—IGS, Wang et al. 2007) show that the mean global difference between IGS and COSMIC TCWV is about -0.2 mm with a standard deviation of 2.7 mm (Fig. 2.24).

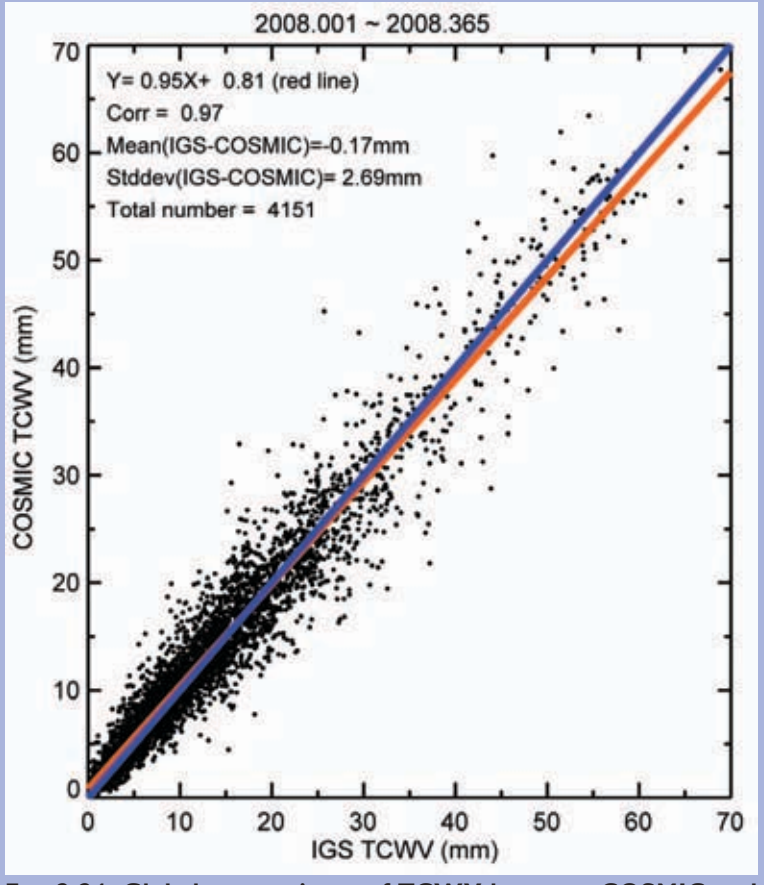

Fig. 2.24. Global comparisons of TCWV between COSMIC and those derived from ground-based GPS (i.e., IGS) for 2008.

6) Lake levels—C. Birkett

Lake volumes respond to changes in precipitation integrated over their catchment basins (Street-Perrott et al. 1986) and are indirect indicators of climatic change (Langbein 1961; Szesztay 1974). The response is particularly marked for closed lakes (having no significant surface or subsurface outflow) whose surface area, when in hydrological equilibrium, has been used in paleoclimatic studies to indicate changes in aridity. Closed lakes act as low-pass filters to variations in aridity, with a characteristic time constant of between 1 and 1000 years, depending largely on lake geomorphology (Mason et al. 1994). Historical studies of the links between climate and lake levels have concentrated on individual lakes or regions. However, both natural and anthropogenic climate effects have highlighted the need for a global approach to the systematic monitoring of lake levels (Williams 1993). For many lakes ground-based lake levels ('stage') can be difficult to acquire, and while satellite-based imagery can reveal surface extent, there are currently no operational products.

Satellite-based lake-level products, however, are now being offered within three programs (NASA/USDA, ESA, and LEGOS; Fig. 2.25). Records are now long enough in theory to support climate monitoring. Large-lake levels are derived using several satellite radar altimeters with varying temporal (10-, 17-, 35-day) and spatial resolutions. Errors relative to ground-based gauge data can range from a few centimeters to tens of centimeters RMS (Birkett 1995). The NASA/CNES suite of instruments offers measurements from 1992, the ESA suite from 1994. The number of lakes considered varies within each program but Fig. 2.26 shows the potential spatial distribution of all lake products within the NASA/USDA program. Location and lake type information can also be found in the databases of Birkett and Mason (1995, lakes of surface area ≥ 100 km^2) and Lehner and Döll (2004, surface areas ≥ 50 km^2).

While the NASA/USDA program provides a graphic comparison of the near-real-time water level status with respect to a short-term mean (Fig. 2.27), published research has focused more on single basin studies or regional water level variations and their links to ENSO and Indian Ocean SST anomalies (Birkett et al. 1999; Arpe et al. 2000; Mercier et al. 2002; Bergonzini et al. 2004; Zola and Bengtsson 2006; Ricko et al. 2009, manuscript submitted to *J. Climate*). Although the focus in these studies is on larger, open lakes (having significant surface or subsurface outflow), the ability of these phenomena to gain a rapid reaction in lake level regardless of anthropogenic controls shows that global and regional studies should not exclude other lake types and reservoirs.

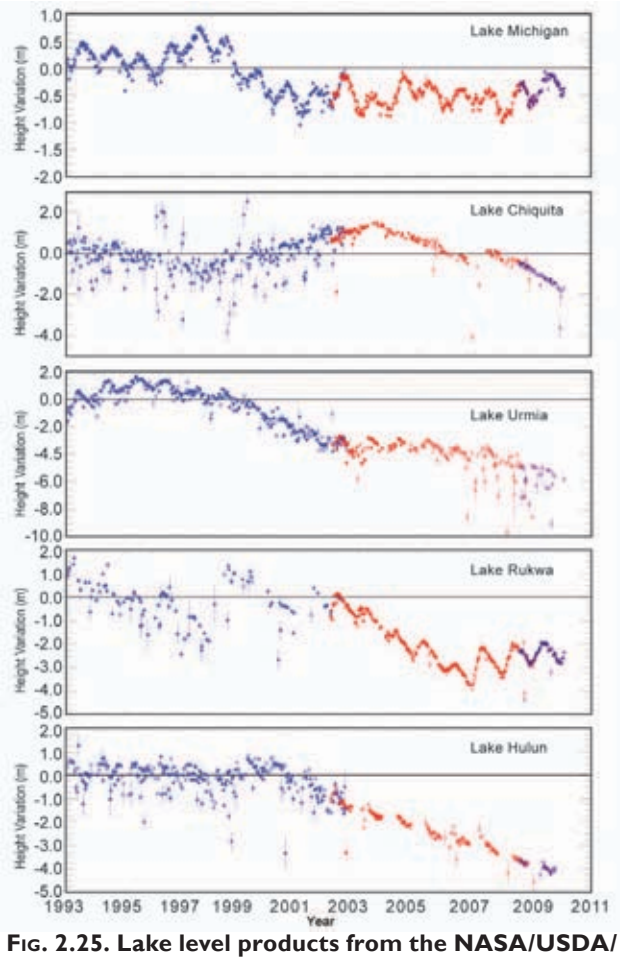

Fig. 2.25. Lake level products from the NASA/USDA/FAS. Topex/Poseidon (blue), Jason-1 (red), and Jason-2 (purple) radar altimeters. The lakes reside in the United States (Michigan), Argentina (Chiquita), Iran (Urmia), Tanzania (Rukwa), and China (Hulun).

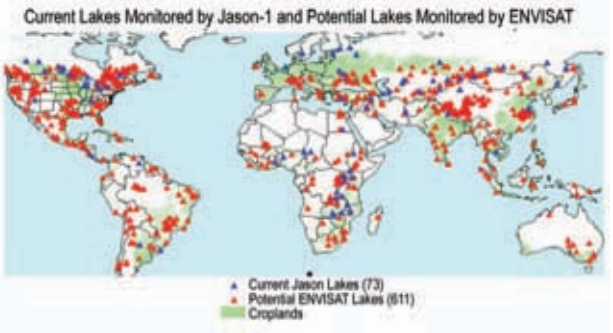

Fig. 2.26. Locations of lakes and reservoirs for which near-real-time lake level products are or will be available through the NASA/USDA/FAS Web site.

Fig. 2.27. Map showing location of currently available NASA/USDA/FAS lake level products depicting the near-real-time lake level status with respect to a short-term mean (1992–2002): red (low water), navy (high water), white missing data .

d. Atmospheric circulation

1) Mean sea level pressure—R. Allan

As highlighted in previous sections, a weak–moderate El Niño event developed mid-2009 following the collapse of La Niña early in the year. As a consequence, the annual global MSLP field showed no distinct El Niño signature (Plate 2.1).

El Niño and La Niña events can be measured by the Southern Oscillation Index (SOI), the normalized MSLP difference between Tahiti and Darwin (Allan et al. 1996). El Niños (negative SOI) and La Niñas (positive SOI) vary in magnitude, duration, and evolution, with no two events or episodes exactly the same. The SOI since 1900 is dominated by interannual to multidecadal vacillations, but very long-term trends are not evident (Fig. 2.28a). The SOI trace since 2000 highlights the shift from the La Niña of 2007/08 to the El Niño of 2009 (Fig. 2.28b). Major El Niño and La Niña events can be near-global in their influence on world weather patterns, owing to ocean–atmosphere interactions across the Indo-Pacific region with teleconnections to higher latitudes in both hemispheres.

The other major event in 2009 was the development of an extreme negative North Atlantic Oscillation (NAO)/Arctic Oscillation (AO) phase in December 2009 that persisted through much of the 2009/10 winter. In Fig. 2.29, the December 2009 global MSLP field distinctly shows the NAO/AO influence

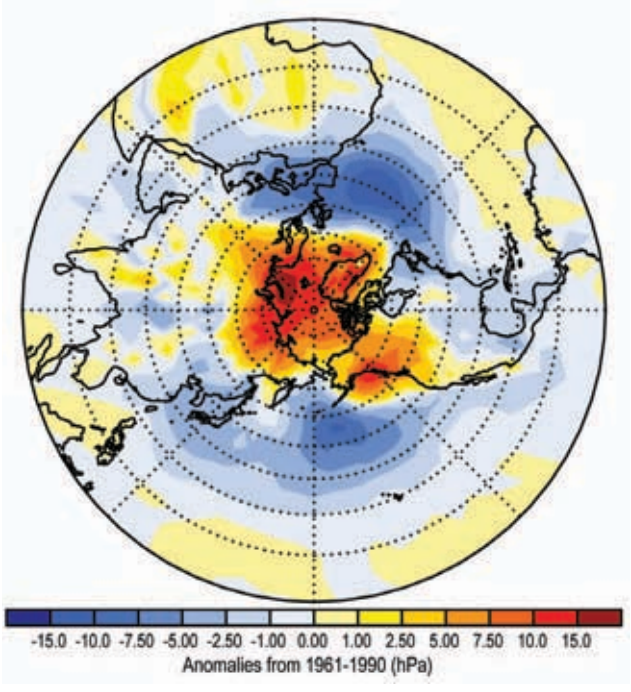

Fig. 2.29. Global MSLP anomalies (hPa) for December 2009 from HadSLP2r (Allen and Ansell 2006).

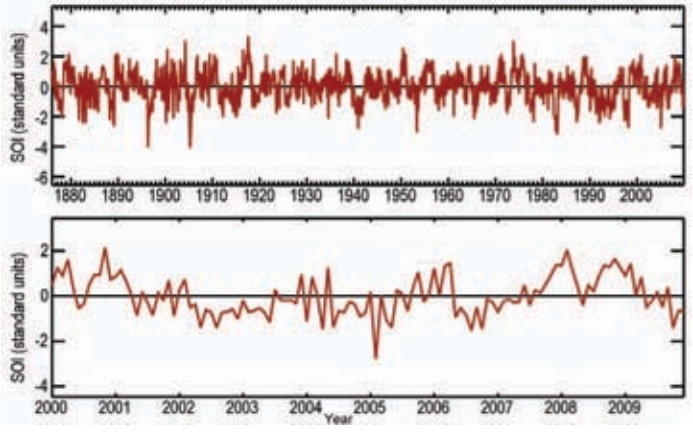

Fig. 2.28. The Australian Bureau of Meteorology SOI for (top) 1876 to 2009 and (bottom) from 2000 to 2009 relative to the 1876 to 2009 average.

across the North Atlantic and North Pacific with positive pressure anomalies over higher latitudes and negative anomalies over the mid-latitudes and an associated reduction in westerlies. This is further evident in Fig. 2.30a which highlights the major shift in atmospheric circulation in early December 2009 which led to record snow and cold temperatures across the UK and parts of Europe and North America. Monthly AO values since 1950 (Fig. 2.30b) indicate that the December 2009 value was the lowest December value in that record.

2) Surface wind speed—C. Mears

Surface wind speed over the world's oceans began to be monitored continuously with

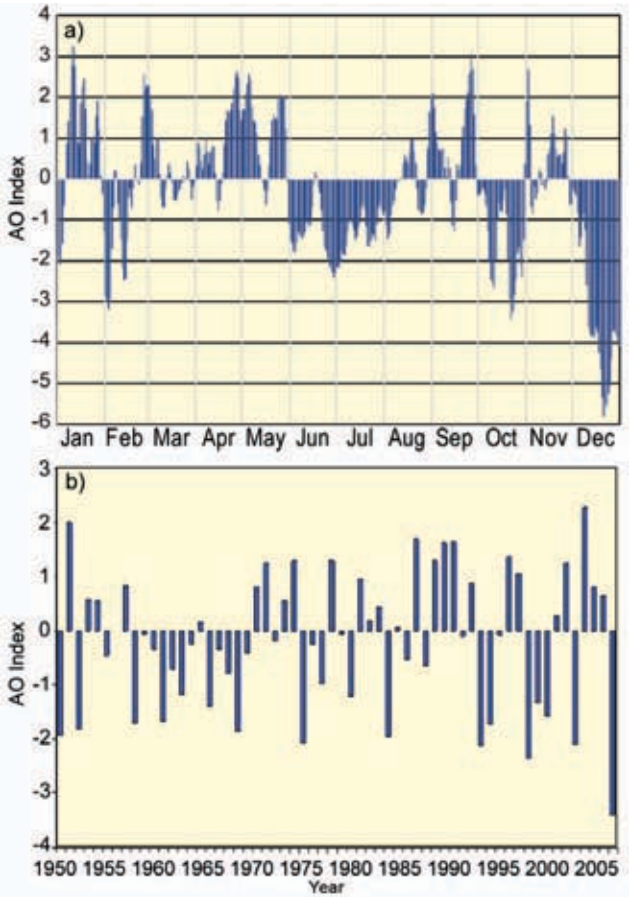

Fig. 2.30. (a) The daily AO index from 31 Aug 2009 to 29 Dec 2009 is constructed by projecting the daily (00Z) 1000mb height anomalies poleward of 20°N onto the loading pattern of the AO. The loading pattern is defined as the leading mode of an EOF analysis of monthly mean 700-hPa height anomalies onto the EOF mode. (b) Constructed as in (a) for monthly December values.

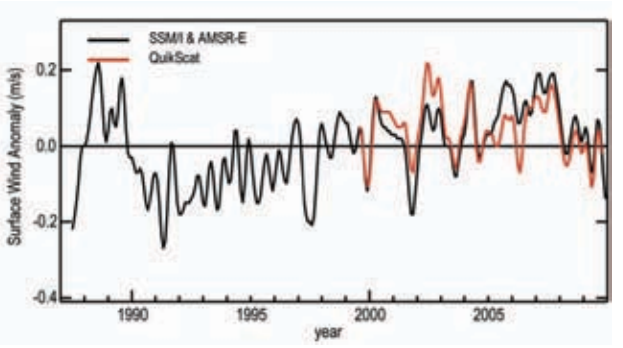

Fig. 2.31. Surface wind speed anomalies over the global ice-free oceans as measured by Remote Sensing Systems from the SSM/I and the Advanced Microwave Scanning Radiometer EOS (AMSR-E) instruments. The time series has been smoothed to remove variability on time scales shorter than 4 months. The reference period for the combined AMSR-E and SSM/I measurements is 1988–2007. For the QuikSCAT measurements the reference period is 2000–2007, with the mean adjusted to match the SSM/I anomalies for 2000–07.

the launch of the first Special Sensor Microwave/Imager (SSM/I) satellite in late 1987. The SSM/I instrument is a microwave radiometer that makes measurements of upwelling microwave radiation to infer the surface roughness of the worlds oceans and thus, the surface wind speed (Wentz 1997). Since the first SSM/I instrument, a number of additional microwave imaging sensors have been launched and intercalibrated to the accuracy necessary for climate studies (Wentz et al. 2007). Globally-averaged winds (Fig. 2.31) exhibited a maximum in 1988/89, followed by a minimum in 1991, and then an increasing trend in global winds from 1990 to 2007. In 2008 and 2009, global wind speed fell slightly. Wind speeds derived from the QuikSCAT microwave scatterometer (Lungu and Callahan 2006), carried on a different satellite than the SSM/I instrument, using a different measurement technology show nearly identical results. Surface wind speed is dominated by short-term variability making it difficult to discern long-term trend behavior.

Winds in the tropics, especially the central tropical Pacific, were sharply reduced during 2009 (Fig. 2.32, Fig. 2.33), as the tropical pacific transitioned to El Niño. Positive wind anomalies in the Atlantic around 45°N coincided with a negative phase of the NAO/AO (Hurrell et al. 2003; Fig. 2.30b) during much of 2009 (Plate 2.1, Fig. 2.33).

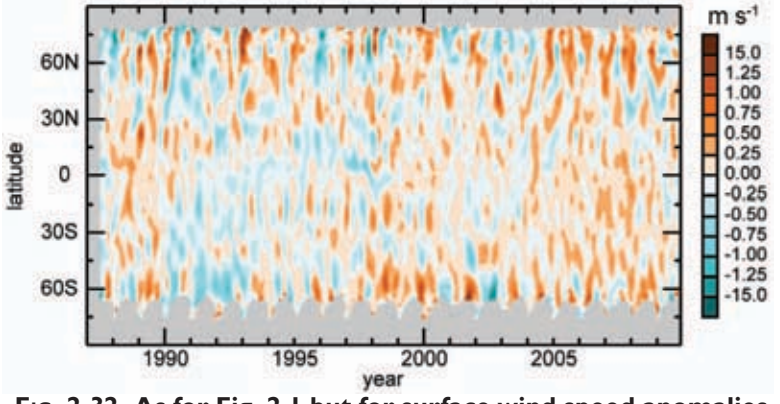

Fig. 2.32. As for Fig. 2.1 but for surface wind speed anomalies (reference period 1988–2007) over the ice-free oceans. Data have been smoothed in time to remove variability on time scales shorter than 4 months.

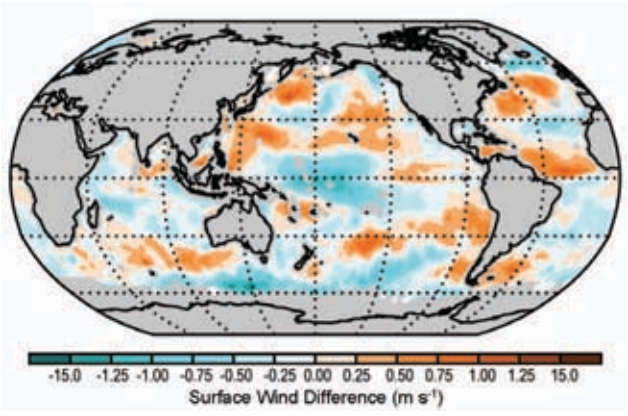

Fig. 2.33. Map of the difference in annual mean wind speed, 2009 minus 2008 calculated using data from AMSR-E.

e. *Earth radiation budget at top-of-atmosphere*—P. W. Stackhouse, Jr., T. Wong, N. G. Loeb, D. P. Kratz, A. C. Wilber, D. R. Doelling, and L. C. Nguyen

Preliminary analysis suggests that both the global-annual mean outgoing longwave radiation (OLR) and the reflected shortwave radiation increased slightly by ~0.1 W m^{-2}, from 2008 to 2009 (Table 2.4). There was very little annual average change in the total solar irradiance (< 0.01 W m^{-2}) since the solar activity remained at minimum during the period. Thus, the combined longwave and shortwave changes caused a reduction of ~0.2 W m^{-2} in total net radiation into the Earth climate system in 2009. These initial results derived from the Clouds and the Earth's Radiant Energy System (CERES; Wielicki et al. 1998) Fast Longwave and Shortwave Radiative Fluxes (FLASHFlux) dataset (Stackhouse et al. 2006; L'Ecuyer et al. 2008) may still include small instrument drift artifacts between January 2008 and December 2009. Reassessments of these results are expected in the forthcoming CERES Edition 3 instrument calibration data and after CERES FLASHFlux is upgraded to provide global gridded monthly anomaly information. Relative to the multiyear dataset average for 2001 to 2008, the 2009 global-annual mean anomaly (Table 2.4) is -0.4/0.0/+0.4 W m^{-2} for longwave/shortwave/total net radiation, respectively. These are within their corresponding 2-sigma interannual variabilities for this period.

Global monthly deseasonalized anomalies since March 2000 have been constructed by merging Earth Radiation Budget (ERB) datasets from two sources: a new CERES SSF (Single Scanning Footprint) 1x1 Degree Lite (SSF 1Deg Lite; a Top-of-Atmosphere [TOA] only version) using the Edition 2.5 instrument calibration; and CERES FLASHFlux (Fig. 2.34). TOA Fluxes from both datasets in the year 2007 were used to normalize the FLASHFlux data to SSF 1Deg Lite. The 2-sigma monthly uncertainty from the overlapped period is ±0.4/±0.9/±1.3 W m^{-2} for the longwave/shortwave/net radiation, respectively. By mid-2009, the decrease in the OLR and the increase in the total net TOA flux continuing from late 2008 peaked and then reversed sign. Smoothed averaged TOA OLR shows a general agreement in fluctuations with a similarly smoothed Multivariate ENSO Index where the index peaked negatively in late 2008/early 2009 and reversed sign during the year. Thus, it appears that change in El Niño intensity is largely responsible for the global averaged monthly TOA variability during this time period. Linear trend analyses are not recommended due to the natural fluctuation in ERB relating to ENSO activity in the short record, large uncertainty from the data merging process, and instrument drift potential in the FLASHFlux data. A long-term homogeneous data source with in-depth instrument stability analysis is needed to reduce these uncertainties for future reassessment activity.

f. Atmospheric composition

1) Atmospheric chemical composition—R. C. Schnell

(i) Carbon dioxide, methane, and carbon monoxide—E. J. Dlugokencky

(A) Carbon dioxide (CO_2)

Since 1750, ~335 billion tons of carbon has been emitted into the atmosphere by human activities, about half of this since the mid-1970s (Marland et al. 2008), and emissions rates increased by > 3% from 2000–04 (Raupach et al. 2007). Atmospheric CO_2 has increased from about 280 ppm at the start

Table 2.4. Summary of the 2009 global-annual mean TOA radiative flux component (W m^{-2}) changes relative to 2008 and the 2001–2008 climatology. TOA Total Net = Incoming (SW) – Outgoing (SW+LW).

	2009 minus 2008	2009 anomaly (relative to a 2001-08 climatology)	2-sigma Interannual variability 2001 to 2008
Outgoing Longwave	0.1	-0.4	±0.6
Reflected Shortwave	0.1	0.0	±0.4
Total Net (>0 into system)	-0.2	0.4	±0.6

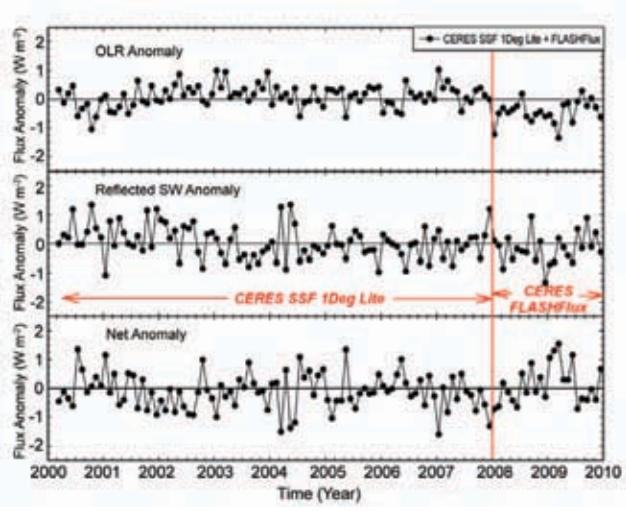

Fig. 2.34. Time series of global-monthly mean deseasonalized anomalies of TOA Earth Radiation Budget for longwave (top panel), shortwave (middle panel), and net radiation (bottom panel) from March 2000 to December 2009. Anomalies are computed relative to the calendar month climatology derived for the March 2000 to December 2009 period. The vertical red line in the figure separates the portion of the time series that is constructed using the CERES SSF 1Deg Lite (3/2000 to 12/2007) and the CERES FLASHFlux (1/2008 to 12/2009) dataset, respectively. Mean differences between datasets were removed using available data from the overlap year 2007 and the combined ERB time series was anchored to the absolute value of CERES SSF 1Deg Lite before deseasonalization (Source: The official data file name of the CERES SSF 1Deg Lite is CER_SSF1deg_month-lite and is available at http://science.larc.nasa.gov/ceres/).

of the industrial revolution to more than 380 ppm today. About half of the emitted CO_2 remains in the atmosphere after a year, and after a millennium, ~20% remains (Archer and Brovkin 2008).

The preliminary globally averaged atmospheric CO_2 mole fraction in 2009 was 386.29 ppm; 1.5 ppm more than 2008 [see Conway et al. (1994) for a description of sampling network and methods]. This is slightly greater than the average rate of increase from 1979 through 2008 of 1.63 ppm yr^{-1}. Despite fossil CO_2 emissions being predominantly in the northern hemisphere, the rate of increase of atmospheric CO_2 is approximately geographically uniform (Fig. 2.35). The amplitude of the seasonal cycle varies based on exposure of air masses arriving at the sites to the terrestrial biosphere, but there are no significant differences in long-term trends.

(B) Methane (CH_4)

After a decade of near-zero growth, atmospheric methane increased globally in 2007 and 2008 by ~7.5 ppb yr^{-1} (Rigby et al. 2008; Dlugokencky et al. 2009), mostly from emissions in the Arctic in 2007 and Tropics in 2007 and 2008. Likely drivers for increased emissions are anomalously high temperatures and precipitation in wetland regions, particularly in the Arctic during 2007. In 2009, globally averaged atmospheric CH_4 increased again (by 6.5 ppb) to 1793.9 ppb, but the main drivers of the continued increase are unclear. The current atmospheric CH_4 observing network, including in situ and remotely-sensed observations, is insufficient to determine with certainty the causes of CH_4 increases over the past three years (see Fig. 2.35).

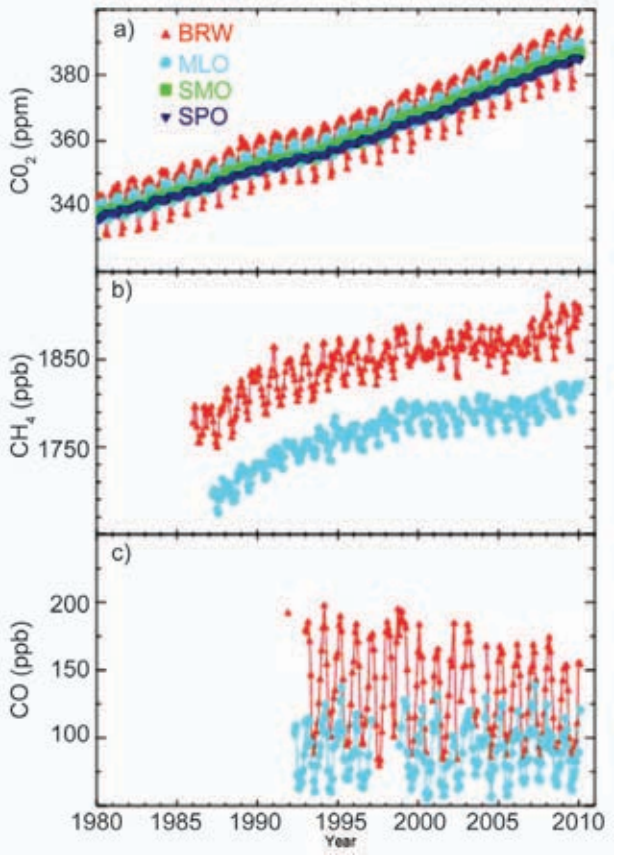

Fig. 2.35. Monthly mean mole fractions determined from NOAA/ESRL Observatories at Barrow, Alaska (BRW); Mauna Loa, Hawaii (MLO); American Samoa (SMO); and South Pole (SPO) for (a) CO_2, (b) CH_4, and (c) CO. 2009 results are preliminary. Monthly means are courtesy of Kirk Thoning (CO_2), Ed Dlugokencky (CH_4), and Paul Novelli (CO), all from NOAA/ESRL. Additional plots can be found at http://www.esrl.noaa.gov/gmd/ccgg/iadv/ and http://www.esrl.noaa.gov/gmd/Photo_Gallery/GMD_Figures/ccgg_figures/.

(C) Carbon monoxide (CO)

There has been no long-term CO trend since ESRL measurements began in 1990 (Novelli et al. 2003), but CO anomalies occurred during 1997 to 1998, and again in 2002 to 2003. These anomalies are likely the result of tropical (Langenfelds et al. 2002) and boreal biomass burning (Kasischke et al. 2000). Since the lifetime of CO is relatively short (few months), the CO enhancements quickly disappeared. The preliminary globally averaged CO mole fraction in 2009 is 80 ppb, 15 ppb lower than 1998. ESRL's surface sampling network is less sensitive to biomass burning emissions of CO than remotely sensed CO observations, such as MOPITT (Measurements Of Pollution In The Troposphere; Pan et al. 1998), because emissions are rapidly transported away from the surface where the sampling sites are. The combination of surface measurements and MOPITT retrievals provide useful auxiliary information in determining the contribution of biomass burning to recent increases in atmospheric CH_4 (see Fig. 2.35).

(ii) Changes in atmospheric abundances of ozone-depleting gases and their replacements—S. A. Montzka and G. S. Dutton

Long-lived halocarbons affect the radiative balance of the atmosphere because they efficiently absorb terrestrial infrared (IR) radiation. Those containing bromine (Br) and chlorine (Cl) also influence the radiative atmospheric balance indirectly through their destruction of stratospheric ozone. Through amendments and adjustments to the 1987 Montreal Protocol on Substances that Deplete the Ozone Layer, the decline in mixing ratios of most of the potent ozone-depleting gases continued in 2009 (Fig. 2.36). However, mixing ratios of some halogenated gases continue to increase globally. The most rapid increases are observed for hydrochlorofluorocarbons (HCFCs) and hydrofluorocarbons (HFCs), common replacements for chlorofluorocarbons (CFCs), halons, and other ozone-depleting gases. Increases in HCFCs have recently accelerated owing to enhanced use in developing countries (Montzka et al. 2009). Both HCFCs and HFCs are efficient absorbers of infrared radiation (Table 2.5). HCFCs contain chlorine but have smaller influence on ozone than the CFCs; HFCs do not cause ozone destruction.

The influence of halocarbon trace-gas trends on future levels of stratospheric ozone can be estimated from weighted sums of Cl and Br in long-

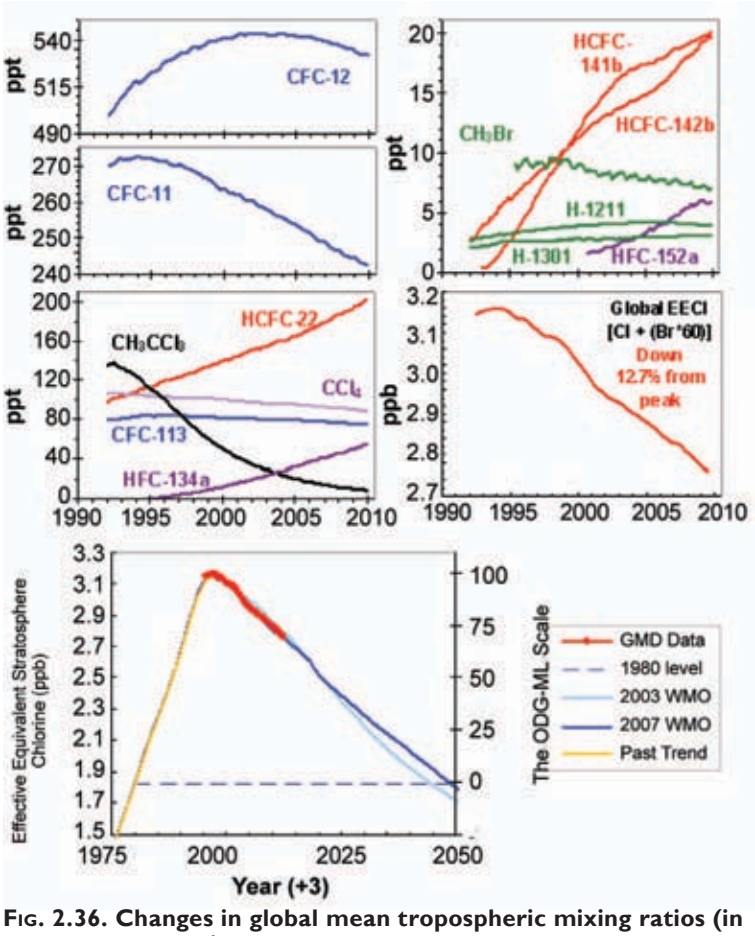

Fig. 2.36. Changes in global mean tropospheric mixing ratios (in ppt, or pmol mol^{-1}) of the most abundant CFCs, HCFCs, HFCs, chlorinated solvents, and brominated gases. The middle-right hand panel shows secular changes in atmospheric effective equivalent chlorine (EECl; in ppb or nmol mol^{-1}), which is an estimate of the ozone-depleting power of these atmospheric halocarbons. EECl is derived from observed mixing ratios of ozone-depleting gases appearing in the other 4 panels, and it is derived from the sum of [Cl + (Br^{x}60)] contained in these gases. The bottom panel shows the recent changes in Effective Equivalent Stratospheric Chlorine (EESC) observed by the NOAA/GMD global network relative to the secular changes observed in the past, including the level observed in 1980 when the ozone hole was first observed, and a projected future. The Ozone Depleting Gas Index for midlatitudes is derived (right-hand axis) from rescaling EESC. EESC is derived from EECl by simply adding 3 years to the time axis to represent the lag associated with mixing air from the troposphere to the middle stratosphere, where the ozone layer resides [Source: updates to Montzka et al. (1996, 1999).]

lived halocarbons. In the midlatitudes, this influence is expressed as effective equivalent chlorine (EECl; Fig. 2.36) and is derived from surface-based measurements. It provides an estimate of the near-future ozone-depleting power of trace gases (EESC, Fig. 2.36), when air at the Earth's surface will have become mixed into the midlatitude stratosphere. A second metric, equivalent chlorine (ECl, not shown), provides an estimate of the ozone-depleting power of trace gases in the near future for the stratosphere over the Polar Regions.

The EECl content of the lower atmosphere has declined fairly steadily since the peak in 1994 through 2009 at a mean rate of 28 ppt yr^{-1}. Despite these substantial changes, full recovery of stratospheric ozone is not expected until the middle to latter part of the 21st century owing to the long lifetime of many of these chemicals (lower panel of Fig. 2.36; Table 2.5). Progress towards EECl reductions can now be readily assessed with the NOAA Ozone-Depleting Gas Index (ODGI) (Hofmann and Montzka 2009). In 2009 the ODGI for the midlatitudes was 68.7 and the ODGI for Antarctica derived from ECl estimates was 83.5 (not shown).

(iii) The combined influence of long-lived trace gases on the radiative balance of the atmosphere—S. A. Montzka

Long-lived trace gases have a direct and indirect influence on the energy balance of the atmosphere. The direct radiative influence of a trace gas is proportional to its atmospheric abundance and its radiative efficiency (Table 2.5). High precision measurements of the major long-lived greenhouse gases and 15 minor greenhouse gases (Table 2.5) have been used to calculate the overall change in the direct radiative climate forcing (Hofmann et al. 2006) (Fig. 2.37). By mid-2008, the increases in the abundances of all these gases amounted to an additional direct radiative forcing to the atmosphere totaling approximately 2.74 W m^{-2}, changes in the abundance of CO_2 accounting for 63% of this enhanced radiative forcing.

The NOAA Annual Greenhouse Gas Index (AGGI)(Hofmann et al. 2006) is calculated as a ratio relative to the direct radiative forcing calculated from these gases for 1990; indirect effects (e.g., arising from ozone depletion or water-vapor feedbacks) are not considered. Preliminary data indicated that the 2009 AGGI was 1.275 (Fig. 2.37) and CO_2 had accounted for about 80% of the observed increase since 1990.

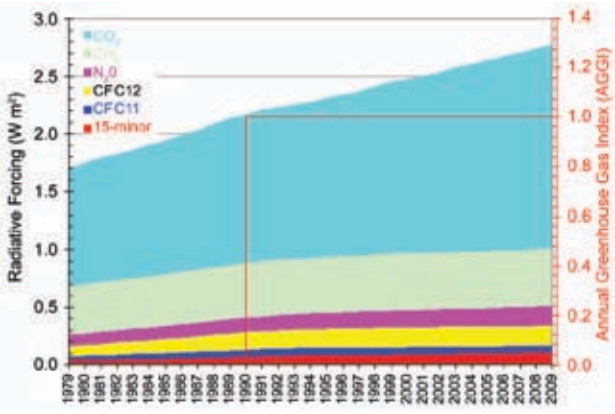

Fig. 2.37. The NOAA Annual Greenhouse Gas Index (AGGI) shows radiative forcing relative to 1750, of all the long-lived greenhouse gases indexed to 1 for the year 1990. Since 1990, radiative forcing from greenhouse gases has increased 27.5%.

(iv) Nitrous oxide (N_2O) and sulfur hexafluoride (SF_6)—J. W. Elkins and G. S. Dutton

Nitrous oxide (N_2O) and sulfur hexafluoride (SF_6) are important atmospheric trace gases with significant man-made sources. Nitrous oxide has the third strongest anthropogenic climate forcing after CO_2 and CH_4 and is considered a major greenhouse gas (Butler 2009). Atmospheric N_2O is also responsible for stratospheric ozone depletion by providing a source of stratospheric nitric oxide (Ravishankara et al. 2009). The 2009 mean global concentration of N_2O was 322.5 ± 0.1 ppb yr^{-1} (Fig. 2.38, top panel). Its mean global growth rate since 1977 is 0.733 ± 0.002 ppb but with substantial interannual variation (Fig. 2.38, bottom panel). The atmospheric N_2O budget is out of balance by one-third as a result of man-made emissions, primarily through emissions from nitrogen fertilizers (Crutzen et al. 2007).

Sulfur hexafluoride has one of the strongest Global Warming Potentials (GWP) of all trace gases at 23 900 times CO_2 with a 100-yr time horizon (Solomon et al. 2007) with the fifth strongest climate forcing of the 10 minor greenhouse gases (Hofmann et al. 2006). Its global average concentration for 2009 was 6.76 ± 0.07 parts-per-trillion dry by mole fraction (ppt) (Fig. 2.38, top panel) and thus its climate forcing contribution is small. The atmospheric lifetime of SF_6 is long (3200 yr); so, many developed countries have instituted voluntary programs with suppliers and utilities to reduce their emissions. The global atmospheric growth rate peaked at 0.32 ppt yr^{-1} in 2008 but in 2009 decreased, perhaps as a result of the recent global economic recession and voluntary efforts by countries to reduce emissions (Fig. 2.38, bottom panel).

Table 2.5. Mixing ratios, radiative efficiencies and lifetimes of chemicals considered in the AGGI.

Industrial Designation or Common Name	Chemical Formula	AGGI	ODGI	Radiative Efficiency (W m^{-2} ppb^{-1}) *	Mean suface mixing ratio mid-2009 [change from 2008 to 2009][a]	Lifetime
Carbon Dioxide	CO_2	Y	N	1.41×10^{-5}	386.3[1.5]	NA
Methane	CH_4	Y	N	3.7×10^{-4}	1.79 [6.5×10^{-3}]	9.0
Nitrous oxide	N_2O	Y	N	3.03×10^{-3}	322.5[0.6]	114
Chlorofluorocarbons						
CFC-11	CCl_3F	Y	Y	0.25	243.3[-1.8]	45
CFC-12	CCl_2F_2	Y	Y	0.32	532.6[-3.0]	100
CFC-113	CCl_2FCClF_2	Y	Y	0.30	75.9[-0.5]	85
Hydrochlorofluorocarbons						
HCFC-22	$CHClF_2$	Y	Y	0.20	198.4[8.7]	12.0
HCFC-141b	CH_3CCl_2F	Y	Y	0.14	19.8[0.6]	9.3
HCFC-142b	CH_3CClF_2	Y	Y	0.20	19.4[1.1]	17.9
Hydrofluorocarbons						
HFC-134a	CH_2FCF_3	Y	N	0.16	52.5[4.8]	14
HFC-152a	CH_3CHF_2	N	N	0.09	5.9[0.3]	1.4
Chlorocarbons						
Methyl Chloroform	CH_3CCl_3	Y	Y	0.06	9.2[-1.6]	5.0
Carbon Tetrachloride	CCl_4	Y	Y	0.13	89.4[-1.4]	26
Methyl Chloride	CH_3Cl	N	Y	0.01	542[-2]	1.0
Bromocarbons						
Methyl Bromide	CH_3Br	N	Y	0.01	7.3[-0.0-2]	0.7
Halon 1211	$CBrClF_2$	Y	Y	0.30	4.0[-0.05]	16.0
Halon 1301	$CBrF_3$	Y	Y	0.32	3.1[0.02]	65
Halon 2402	$CBrF_2CBrF$	N	Y	0.33	0.45[-0.01]	20
Fully fluorinated species						
Sulfur Hexafluoride	SF_6	Y	N	0.52	6.76[0.26]	3,200

NA = Not applicable; the lifetime of CO_2 cannot be expressed as a single number (Archer and Brovkin 2008).

* Radiative forcings and lifetimes are taken from Daniel et al. (2007) and Clerbaux and Cunnold et al. (2007).

[a] Mixing ratios are measured global surface means determined from NOAA global cooperative sampling network (Hofmann et al. 2006). Changes indicated in brackets are simply the difference between the 2009 and 2008 annual global surface mean mixing ratios. Units are ppm for CO_2, ppb for CH_4 and N_2O, and ppt for all others.

2) Global aerosols—J.W. Kaiser, A. Benedetti, and J.-J. Morcrette

Atmospheric aerosols influence atmospheric radiation and cloud droplet nucleation. Inadequate understanding of these direct and indirect effects dominates uncertainty of the radiative forcing in climate projections from climate models (Alley et al. 2007). The aerosol sources are influenced by changes in land cover, wind and precipitation patterns, and human activities. Global monitoring of aerosols remains a substantial scientific challenge due to their large variability and heterogeneity in chemical composition and size. Current routine ground- and satellite-based observations of aerosols cannot provide high temporal

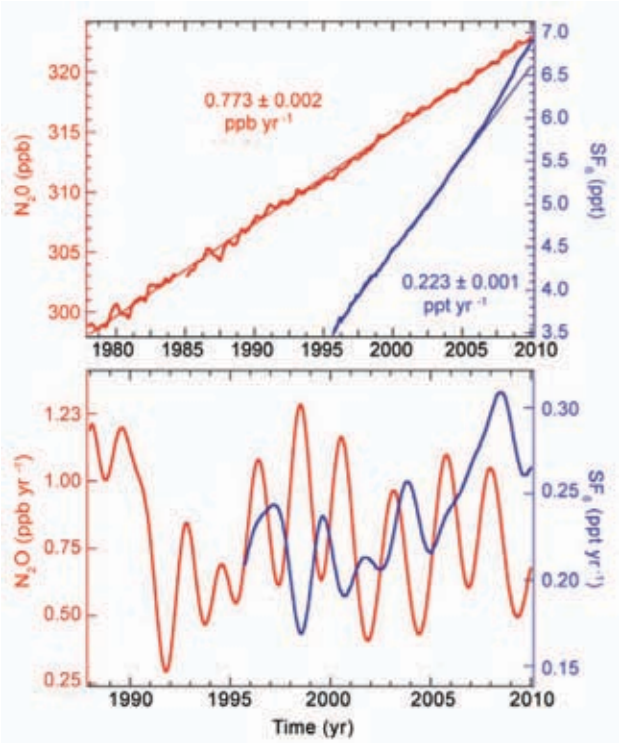

Fig. 2.38. (top) Global monthly means along with estimates for the linear growth rate of atmospheric nitrous oxide (N_2O, red) in ppb and sulfur hexafluoride (SF_6, blue) in ppt from the NOAA/ESRL halocarbon network (binomial smoothing with 3 month filter). (bottom) Instantaneous growth rate of N_2O and SF_6 of data above using a FFT smoothing algorithm (Thoning et al. 1989) with a two year filter, note the rise of the atmospheric SF_6 growth rate after 2003. Atmospheric data for N_2O prior to 1989 and for SF_6 prior to 1999 were analyzed from flasks instead of continuously operating instruments at NOAA/ESRL baseline observatories.

resolution global coverage and yield only very limited information on the chemical composition, size distribution, and vertical profiles.

The Global and regional Earth-system Monitoring using Satellite and in-situ data project (GEMS, Hollingsworth et al. 2008) has created a continuous space-time representation of the global aerosol distribution since 2003. It assimilates 550 nm aerosol optical depth (AOD) observations from Moderate Resolution Imaging Spectroradiometer (MODIS) into ECMWF's numerical weather prediction model extended to include the sources, sinks, and transport and conversion processes of several aerosol species (Benedetti et al. 2009; Morcrette et al. 2009). Monitoring Atmospheric Composition and Climate (MACC), the follow-up project of GEMS, is currently producing real-time aerosol analyses and forecasts and a new reanalysis starting in 2003, both with improved model, emission inventories and data assimilation system. Total AOD is strongly constrained by observations over ocean but over land, the total AOD information is a mix from observations and model. Total AOD at high latitudes and the relative distribution between the aerosol species at all latitudes come largely from the model.

On a global scale, the aerosol distribution up to September 2009 appears to have been in line with previous years back to 2003 (Fig. 2.39). The largest contribution to AOD comes from organic matter, closely followed by sea salt, then dust and sulfate. Dust aerosols have a fairly regular annual cycle with a maximum in the Northern Hemisphere summer. Organic matter varies with a higher frequency and more variability, but less amplitude than dust. Sea salt and black carbon exhibit little variability.

Sea salt aerosols are associated with storms, particularly in the Southern Ocean (Fig. 2.40). Dust is lifted by strong winds from bare soils and deserts; the Sahara, with its dust outflow over the Atlantic, is most pronounced. Organic matter and black carbon are dominantly produced by biomass burning at low-latitudes and to a lesser degree in boreal forests. Even though black carbon has a relatively low AOD, as the most absorbing aerosol type, it has a large impact on atmospheric radiation. The distribution of sulfate aerosols reflects the anthropogenic emission inventory that was used in the model with rather localized sources in North America, Europe, India, and China.

3) Stratospheric ozone—M. Weber and W. Steinbrecht

The 2009 annual mean anomaly of total column ozone was generally positive (compared to the 1996 to

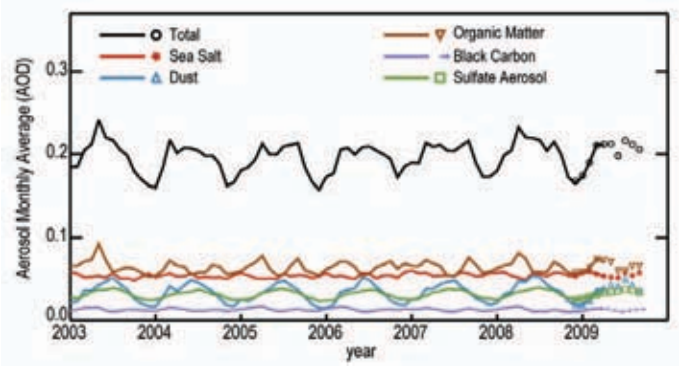

Fig. 2.39. Global, monthly average optical depth at 550 nm of total aerosols for January 2003–September 2009 and the individual contributions of sea salt, dust, organic matter, black carbon and sulfate aerosols. Lines: reanalysis. Symbols: real-time analysis/forecast.

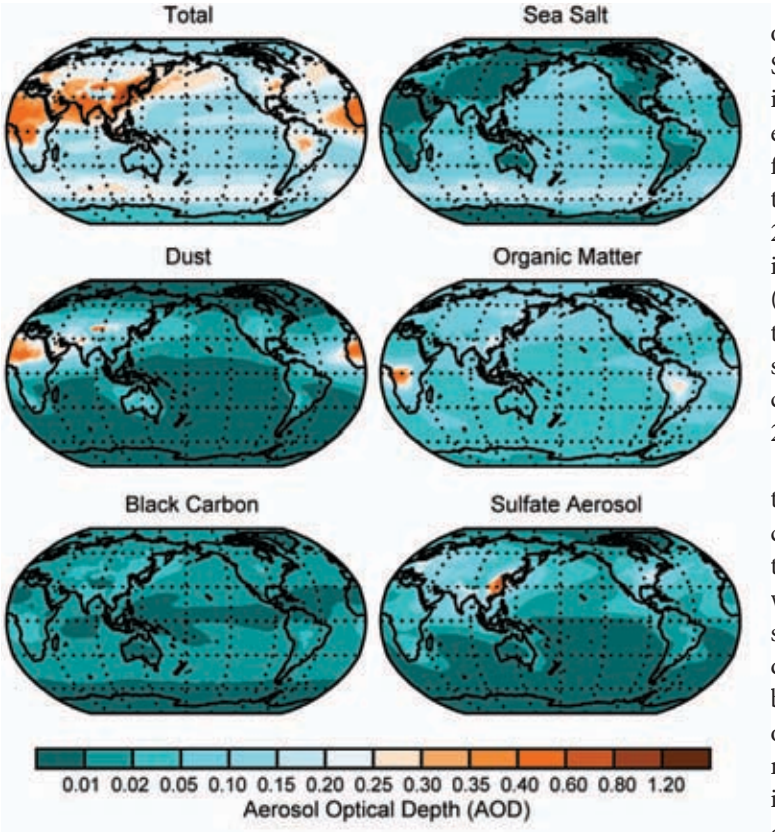

Fig. 2.40. Distribution of average optical depth at 550 nm in 2003–08 of total aerosols and the individual contributions by total, sea salt, dust, organic matter, black carbon and sulfate aerosols.

2009 climatological mean) except for a narrow band in the tropics, a small region over the North Pacific, and above Antarctica (Plate 2.1). Maximum positive anomalies of up to about 20 Dobson Units (DU) occurred at northern mid- to high latitudes, from the North Atlantic to Russia. Positive anomalies were also observed at similar latitudes in the Southern Hemisphere. The largest year-to-year variability is normally observed during winter/spring in each hemisphere. In February and March 2009 positive anomalies of over 50 DU were observed over Europe and Russia and much of the north polar region. However, a region above the Aleutian peninsula, characterized by the Aleutian high, associated with a high tropopause and dynamically reduced column ozone, experienced a -25 DU anomaly. During Arctic winter an unusually large sudden stratospheric warming (SSW) event occurred in January 2009 (Fig. 2.9), contributing to a weaker than usual Arctic vortex and increased ozone transport into high latitudes (Labitzke and Kunze 2009).

Negative anomalies were observed in the tropics within a narrow 20° latitude band around the equator. Interannual modulation of tropical stratospheric ozone is dominated by the QBO (see Section 2b4; Baldwin et al. 2001). During 2009, the QBO phase (stratospheric equatorial winds near 50 hPa) changed from west to east. This led to negative total ozone anomalies in the second half of 2009. The QBO has a periodic signature in tropical (and extratropical) total ozone (Fig. 2.41). Plate 2.1 and Fig. 2.41 show that the 2009 Antarctic ozone hole was slightly larger than the long-term mean, comparable to 2007, but not as large as in 2008, or in the record year of 2006.

The trend in the global annual mean total ozone (Fig. 2.42a) has its main contribution from changes at midlatitudes in both hemispheres (Fig. 2.42b,d), while tropical ozone (Fig. 2.42c) does not show a significant trend. The long-term decrease starting in the 1970s slowed by the mid-1990s and has since leveled off in the extratropics. The substantial minimum in the Northern Hemisphere in the mid-1990s is due to intensification of the chlorine induced ozone decline by the Mount Pinatubo volcanic eruption and by a series of unusually cold Arctic winters with reduced ozone transport and high polar ozone loss (Dhomse et al. 2006). It is expected that total ozone should recover since stratospheric halogen has levelled off and is now declining (Section 2f1ii). However, other factors, e.g., changes in the Brewer-Dobson circulation, annular modes of internal variability, or the 11-year solar cycle also contribute to decadal changes (Appenzeller et al.

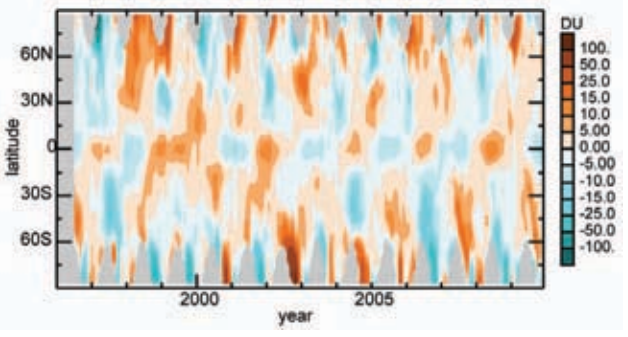

Fig. 2.41. As for Fig. 2.1 but for total ozone anomalies. Anomalies are based on the merged GOME1/SCIAMACHY/GOME2 merged total ozone (Weber et al. 2007). Anomalies were calculated from area weighted monthly mean zonal mean data in 5° latitude steps after removing the seasonal mean from the period 1996–2009.

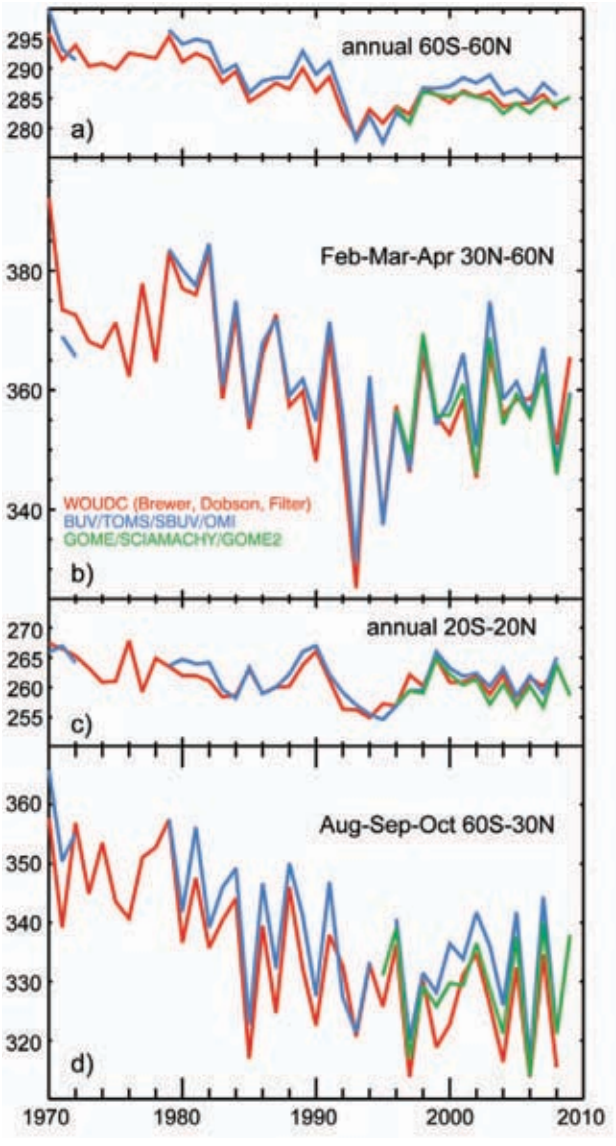

Fig. 2.42. Total ozone time series of ground-based measurements combining Brewer, Dobson, and filter spectrometer data (red, Fioletov et al. 2002), the merged BUV/SBUV/TOMS/OMI (blue, Frith et al. 2004), and GOME1/SCIAMACHY/GOME2 (green, Weber et al. 2007) merged data sets in the (a) 60°N–60°N (annual mean), (b) 30°N–60°N (FMA mean), (c) 20°S–20°N (annual mean), (d) and 60°S–90°S (ASO mean).

2001; Weber et al. 2003; Orsolini 2004; Yang et al. 2005; Dhomse et al. 2006; Stolarski and Frith 2006; Vyushin et al. 2007; Harris et al. 2008).

The upper stratospheric ozone is a better diagnostic to look for ozone recovery because chlorine induced chemical ozone changes there are larger than the changes in column ozone (Newchurch et al. 2003). Also, atmospheric transports play a lesser role. Ozone in the upper stratosphere declined substantially, by 10% to 15%, from the early 1980s to the mid-1990s but has since levelled off (Fig. 2.43). In the last 10 years, the various records show signs of an increase (Steinbrecht et al. 2009; A. Jones et al. 2009). This long-term behavior of ozone in the upper stratosphere is in agreement with the earlier large increase and subsequent decline of the stratospheric halogen load (Fig. 2.36). Superimposed are quasi-

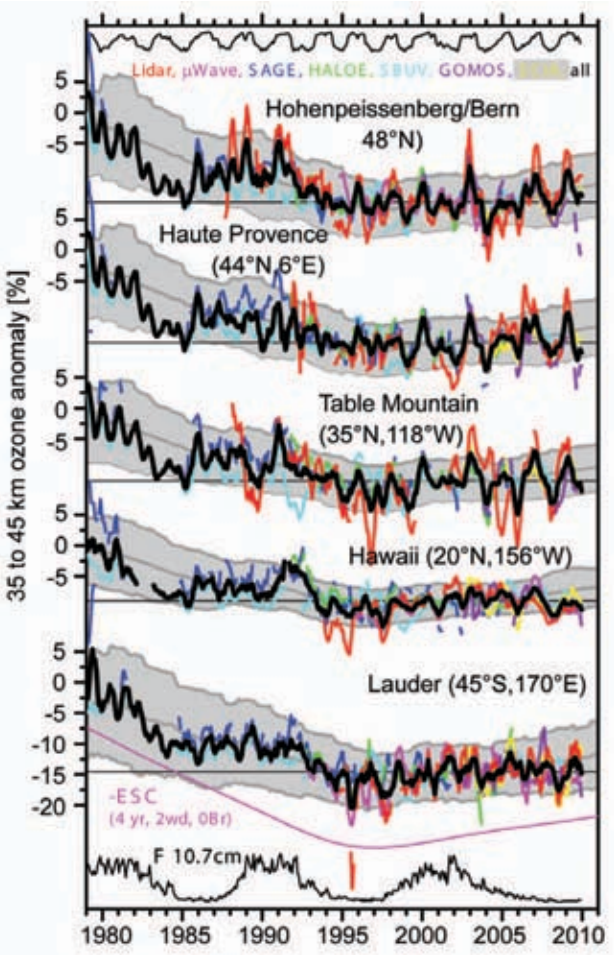

Fig. 2.43. Upper stratospheric ozone anomalies from ground-based stations (lidar, microwave radiometer) and satellite instruments (SBUV, SAGE, HALOE, GOMOS, SCIAMACHY, zonal means within ±5° latitude of the stations). Data are 5-month running mean anomalies (with the 1998 to 2008 climatology subtracted), averaged from 35 to 45 km altitude (Steinbrecht et al. 2009). Scale is shifted, so that the 1979 all instrument average (black line) is at zero. Grey underlay: Mean ±2σ standard deviation of model runs from the CCMVal initiative (Eyring et al. 2006). Black lines at top and bottom: Proxies for QBO and 11-year solar cycle, i.e. negative equatorial wind at 10 hPa (http://www.geo.fu-berlin.de/en/met/ag/strat/produkte/qbo/index.html) and solar radio flux at λ=10.7 cm (http://www.ngdc.noaa.gov/stp/SOLAR/), respectively. Pink line near bottom: Effective stratospheric chlorine (inverted, from Newman et al. 2007, age-of-air: 4±2 years).

biennial and decadal ozone variations, which follow the QBO and the 11-year solar cycle. In late 2009, the QBO phase (beginning westerly at 10 hPa, easterly at 50 hPa, see section 2b4) and the continuing solar minimum both contributed to low levels of upper-stratospheric ozone. On the whole, however, the observed long-term behavior confirms model results with an ongoing slow recovery of upper stratospheric ozone expected.

g. Land surface properties

1) Alpine glaciers and ice sheets—M. S. Pelto

The World Glacier Monitoring Service (WGMS) records of mass balance (difference between accumulation and ablation) and terminus behavior (WGMS 2009; WGMS 2008) provide global indices of alpine glacier behavior. Mass balance was negative in 2008 for the 18th consecutive year. Preliminary 2009 data from Austria, Norway, New Zealand, and the United States indicate it is highly likely that it was the 19th consecutive year of negative annual balances. The worldwide retreat of mountain glaciers is one of the clearest signals of ongoing climate change (Haeberli and Hoelzel 1995).

Alpine glaciers have been studied for more than a century (Oerlemans 1994). The retreat of their termini is a reflection of strongly negative mass balances over the last 30 years (WGMS 2007) which when combined with recent rapid retreat has led to some glaciers disappearing (Pelto 2010).

The cumulative loss of the last 30 years averaged across 30 WGMS reference glaciers is 11.6 m water equivalent (w.e.), equivalent to slicing 13 m off the top of the average glacier (Fig. 2.44). The decadal mean annual mass balance was -198 mm in the 1980s, -382 mm in the 1990s, and -624 mm for 2000–08 (Fig. 2.45). The declining trend is remarkably consistent from region to region (WGMS 2009). A glacier with a sustained negative balance will retreat. Glacier retreat primarily results in the loss of the low-elevation region of a glacier; this potentially reduces total ablation, increases mass balance, and reestablishes equilibrium. Currently, despite sustained negative mass balance and significant glacier retreat, alpine glaciers are not approaching equilibrium. If a glacier experiences significant thinning in the upper regions during this retreat this is symptomatic of not having a sufficient accumulation zone to survive the current climate (Pelto 2010; Paul et al. 2007).

Of 93 Austrian glaciers surveyed in 2009, 85 receded, 7 were stationary, and 1 advanced with a mean terminus change rate of -14.3 m, slightly higher than in 2008. Winter accumulation on Austrian glaciers was about average and summer loss was above average due to higher than normal summer temperatures. The mass balance loss was larger than the decadal mean 1998–2008; Hintereisferner -1182 mm w.e., Kesselwandferner -795 mm w.e., and Jamtalferner -953 mm w.e. (A. Fischer, personal communication).

Over Switzerland 81 of the 88 glaciers examined retreated, 2 advanced, and 5 were stable in 2009. Overall mass balance was negative (Swiss Glacier Monitoring, personal communication).

Preliminary 2009 results indicate normal accumulation and ablation for Norway (L. Andreasson, personal communication). Terminus fluctuation data from 27 glaciers indicates 22 retreating, 3 stable, and 2 advancing with average terminus change of -18 m, compared to -13 m in 2008.

In the North Cascades, Washington, (Pelto 2010) the ENSO transition led to negative mass balances

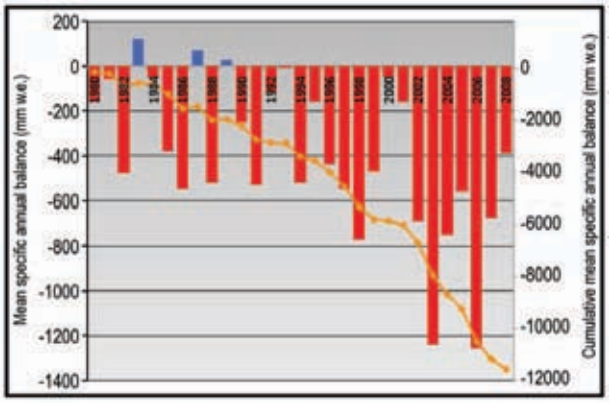

Fig. 2.44. The mean annual balance reported for the 30 reference glaciers to the WGMS (bars) and the cumulative annual balance for the reference glaciers (line).

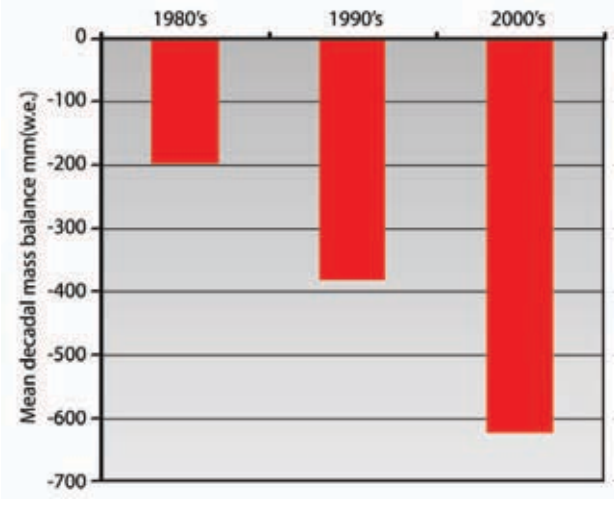

Fig. 2.45. The decadal mean cumulative specific mass balance (mm w.e.) for the 30 reference glaciers.

with all 42 glaciers observed retreating. Winter accumulation during La Niña was near normal, but summer melting as El Niño began was well above average leading to substantial negative balances on all 10 glaciers observed, averaging -1930 mm w.e.

In New Zealand, glaciers shrank between April 2008 and March 2009 owing to above normal temperatures and below normal rainfall in both winter and summer (J. Hendrikx, personal communication). On 50 glaciers surveyed the average snow line was 95 m above the equilibrium snow line elevation, the sixth highest in the 33 year record.

Negative anomalies in melting days occurred in 2009 in South and West Greenland, and positive anomalies in North and East Greenland as derived from SSM/I brightness temperatures relative to the 1979–2008 average (Tedesco et al. 2008). Melt extent was 670 000 km^2, slightly lower than in 2008. Surveys of Greenland marine terminating outlet glaciers from MODIS imagery (J. Box, personal communication) indicate that the 34 widest glaciers collectively lost 106.4 km^2 of ice extent between late summer 2008 and late summer 2009.

A 30-year minimum Antarctic snowmelt occurred during austral summer 2008/09 according to microwave satellite observations. Strong positive phases of the SOI and the Southern Hemisphere Annular Mode were recorded during the months prior to and including the 2008/09 melt season. Wilkins Ice Shelf experienced the highest number of melting days across Antarctica (90 days; Tedesco and Monaghan 2009), ending in the collapse in April 2009 of the last strip of ice connecting Wilkins Ice Shelf to Charcot Island.

2) Fraction of Absorbed Photosynthetically Active Radiation (FAPAR)—N. Gobron, W. Knorr, A. S. Belward, and B. Pinty

The state of vegetation has been monitored using monthly estimates of the FAPAR from NASA/SeaWiFS and ESA/MERIS from 1998 to 2009 (Gobron et. al. 2010, manuscript submitted to *Geophys. Res. Lett.*) FAPAR is largely controlled by Leaf Area Index (which controls attenuation of radiation) and to a lesser extent by the absorption efficiency of the vegetation elements composing the canopy and the soil background brightness (through backscattering processes). In Plate 2.1 the strongest positive anomalies for 2009, indicating favorable vegetation growing conditions, are found in eastern Brazil (Cerrado and Mid-Atlantic coastal region) and South Africa, while most of the rest of South America and east Africa exhibit the strongest negative anomalies. Persistent droughts in Southern America, East Africa, and Australia (WMO 2010) are clearly manifest in poor vegetation growth and vigor. The profound nature of the impact of these droughts is further illustrated in Fig. 2.46, which provides a seasonal breakdown. Figure 2.46 illustrates how the Southern Hemisphere contrasts sharply with the Northern Hemisphere—negative anomalies persist through all seasons in the south, while the north (especially central North America and western Europe) fluctuates between the two states. Pronounced positive anomalies of eastern Brazil are mainly due to FAPAR changes in the Southern Hemisphere winter and spring, i.e., the local dry season. The weaker positive anomaly in southern Africa and the strong negative anomaly in southeastern South America are manifest mainly during December 2008–February 2009. This period was characterized by moderate La Niña conditions. Southern Africa (South Africa, Botswana, and Namibia) exhibits statistically significant negative correlations between SOI (which is positive during La Niña) and observed precipitation, while no known significant teleconnection exists between ENSO and the South American region (van Oldenborgh and Burgers 2005).

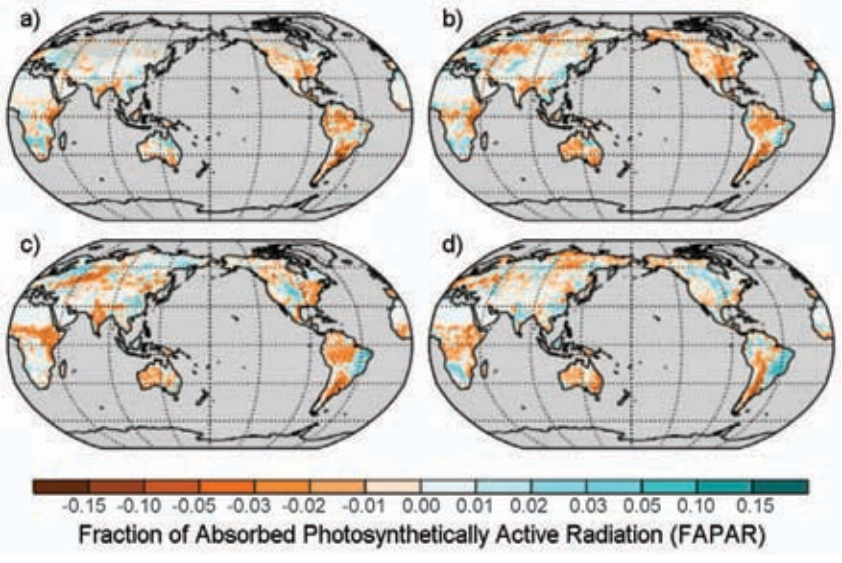

Fig. 2.46. Maps of seasonal FAPAR Anomalies in 2009. Each panel shows the anomalies averaged over the Northern Hemisphere: (a) winter (DJF); (b) spring (MAM); (c) summer (JJA); and (d) fall (SON), respectively.

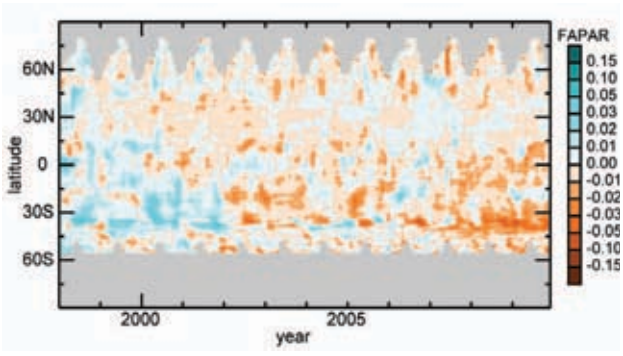

Fig. 2.47. As for Fig. 2.1 but for monthly zonal FAPAR anomalies

Figure 2.47 suggests the presence of a negative trend occurring over the latitude band 30°S to 50°S. This is apparent in the globally averaged time series (Fig. 2.48) and strong enough to yield global monthly negative anomalies for the most recent years. These negative anomalies have been continuous since 2007 reaching a minimum in May 2009. FAPAR is related to CO_2 assimilation by plants. The negative tendency since records began in 1998 indicates that the efficiency of CO_2 assimilation, at least as monitored through the FAPAR proxy of photosynthetic rate, does indeed appear to be declining (Knorr et al. 2007). Both Figs. 2.47 and 2.48 also show that this trend is not merely a result of an anomalous year in 1998. Instead, after the period of FAPAR decline in 2000–03 noted by Knorr et al. (2007), we find another period of similar decline since 2007, interrupted by only a moderate recovery during 2004–07.

3) Biomass burning—J. W. Kaiser and J. G. Goldammer

Vegetation fires (burning of live and dead biomass) and their impacts are influenced by complex interactions between biosphere, humans, and climate (e.g., Bowman et al. 2009). Size, intensity and severity of fires respond to changes of weather and climate (interannual climate variability and long-term climate change). The resulting carbon emissions, e.g., 2.0 Pg C $year^{-1}$–3.2 Pg C $year^{-1}$ in 1997–2004 (van der Werf et al. 2006), can amount to almost half those from fossil fuels, i.e., 7.2 Pg C $year^{-1}$ in 2000–05 (Alley et al. 2007). Therefore, fire must be included in any quantitative model of the global carbon cycle. In ecosystems where regular fires are part of the natural cycle, the released carbon is taken up again by regrowth. If fires result in permanent deforestation or vegetation degradation, on the other hand, carbon stocks may be depleted irreversibly (Fargione et al. 2008). The emitted carbon monoxide and ozone also significantly increase the radiative forcing, while the net effect of the resulting changes in surface albedo reduces it (Bowman et al. 2009). The indirect effect of smoke aerosols is still poorly understood.

The GEMS project and its follow-up MACC (Hollingsworth et al. 2008) derive retrospective and real-time biomass burning emissions from satellite-based observations of Fire Radiative Power (FRP). This is approximately proportional to the biomass combustion rate for open fires (Wooster et al. 2005). Figure 2.49 shows FRP averaged over 2003–08 (a) and for 2009 (b), with five-degree resolution. These are derived from the FRP products of the two MODIS sensors using a cloud cover correction at a resolution

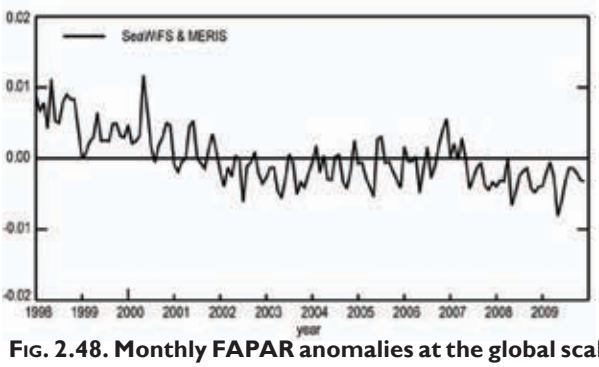

Fig. 2.48. Monthly FAPAR anomalies at the global scale relative to the 1998 to 2009 average.

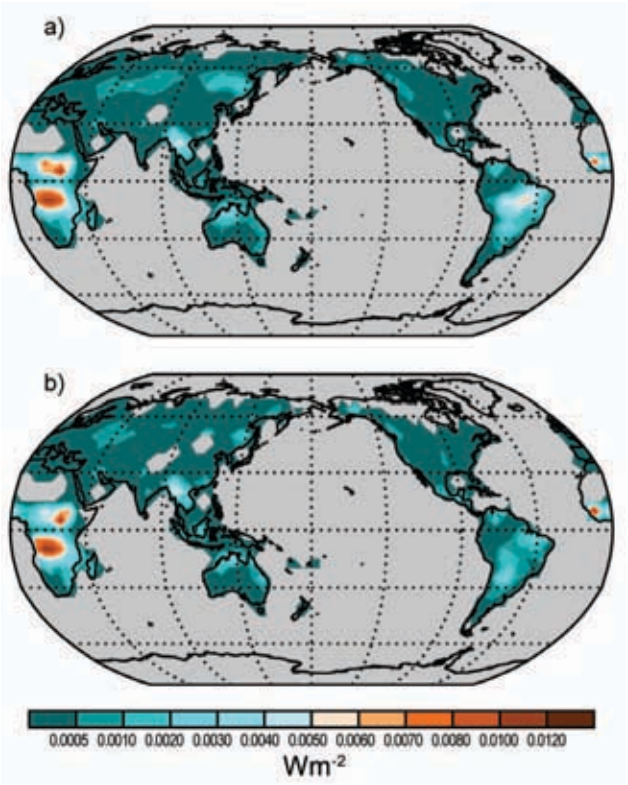

Fig. 2.49. Global fire distribution of 2003–08 (climatology period) (a) and 2009 (b), all in terms average fire radiative power density (W m^{-2}) observed by MODIS.

of 0.1° and 5 days (Kaiser et al. 2009). Validation of the data is still ongoing.

The climatology displays the main burning seasons in Sub-Saharan and Southern Hemispheric Africa, South America, the South-East Asian peninsula, and Australia. Boreal forest fires are only of secondary importance for the global budget. Peat forest fires on South-East Asian islands and understory ground fires are expected to be underrepresented because they are not fully visible from space. Fires detected around the Persian Gulf are flares from oil production instead of biomass burning (cf. Schultz 2002).

Globally, the biomass burning rate of 2009 was the lowest in the short record. Two-thirds of the global reduction has taken place in South America, where Brazil has drastically reduced the deforestation in the Amazon basin (Fig. 2.49/Plate 2.1: see also http://www.obt.inpe.br/prodes/prodes_1988_2009.htm). On-site field exploration by the Global Fire Monitoring Center (GFMC) in the Russian Federation also revealed a significant decrease of wildfires in 2009 as compared to the early 2000s due to prevailing moist weather conditions (http://www.fire.uni-freiburg.de/GFMCnew/2009/10/1014/20091014_ru.htm). Global and regional budgets of FRP are listed in Table 2.6.

Table 2.6. Regional Budgets of Burnt Biomass in terms of Fire Radiative Power.

Region	Climate: average (range) [GW]	2009 [GW]	Change w.r.t. average (%)
Global	132 (125-139)	113	-14
SH Africa	35 (33-36)	34	-1
NH Africa	33 (29-35)	30	-7
C & S America	30 (23-35)	18	-39
SE Asia & Australia	19 (14-23)	18	-1
Northern Asia	11 (8-15)	8	-27
N America	5 (4-5)	4	-18
Europe	3 (2-4)	3	-1